Impact Comparison of Different Aerosol Types on Atmospheric Correction of Landsat 8 over Land

Shuning Zhang [1, 2, 3], Hao Zhang[4], Bing Zhang[3, 4], Zhenzhen Cui[1, 2]

[1]The Key Laboratory of Digital Earth Science, Aerospace Information Research Institute, Chinese Academy of Sciences, Beijing 100094, China;

[2]The International Research Center of Big Data for Sustainable Development Goals, Beijing 100094, China

[3]The College of Resources and Environment, University of Chinese Academy of Sciences, Beijing 100049, China

[4]The State Key Laboratory of Remote Sensing and Digital Earth, Aerospace Information Research Institute, Chinese Academy of Sciences, Beijing 100094, China

Correspondence to: Shuning Zhang (zhangshuning21@mails.ucas.ac.cn)

Abstract. The official Landsat 8 surface reflectance (SR) product, generated by the Land Surface Reflectance (LaSRC) algorithm, is the most extensively utilized medium-resolution dataset and serves as a benchmark to cross-validate the accuracy of other SR products. However, the accuracy of the Landsat 8 SR products did not meet the expectations of the previous studies under specific conditions. Consequently, it is necessary to analyze the Urban Clean aerosol-type assumption implemented in the LaSRC algorithm and comprehensively re-evaluate the accuracy of the Landsat 8 SR. Therefore, this study leverages Landsat 8 data over 600 scenes acquired at 100 Aerosol Robotic Network (AERONET) sites globally and conducts a comprehensive analysis of how different dynamic aerosol types—MOD04-based (used in the Moderate Resolution Imaging Spectroradiometer (MODIS) Atmosphere Level-2 Aerosol Optical Depth Product), MOD09-based (used in MODIS Terra Atmospherically Corrected Surface Reflectance Product), and Urban Clean (used in LaSRC)—affect the accuracy of atmospheric correction (AC) for the first time. The results indicated that, in terms of aerosol optical depth (AOD), the MOD04 aerosol type exhibited the highest accuracy, with a coefficient of determination (R^2_AerT) of 0.7636, Root Mean Square Error (RMSE) of 0.0437, and bias of 0.0052. The accuracy (A), precision (P), and uncertainty (U) of the SR products corresponding to the three aerosol types were within the ranges of -2.9754E-04–3.0145E-03, 2.3185E-02–2.6021E-02, and 2.3367E-02–2.6040E-02, respectively. The MOD04-based aerosol type demonstrated the highest overall accuracy in the visible and near-infrared (VNIR) bands. The MOD09-based aerosol type outperformed the others in the bright surface regions. The Urban Clean aerosol type showed a comparable but slightly inferior performance to that of the MOD09-based aerosol type, with limited advantages in specific reflectance ranges. Moreover, LaSRC-derived SR demonstrated higher stability and accuracy in the shortwave infrared (SWIR) bands compared to its inferior performance in the VNIR. These findings emphasize the critical importance of aerosol-type assumptions in AC workflow. A mixed strategic implementation framework is proposed as follows: (1) adopt MOD04-based aerosol types for AOD retrieval and VNIR SR retrieval, (2) utilize MOD09-based aerosol types to process data acquired over bright surface processing, and (3) leverage

SWIR SR products derived by LaSRC. Our findings provide actionable guidelines for dynamic aerosol-type selection to enhance the AC performance across diverse environments.

1 Introduction

Atmospheric correction (AC), a critical component of remote sensing data processing, aims to mitigate atmospheric scattering and absorption effects on electromagnetic signals and convert sensor-received radiance into accurate surface reflectance (SR). Aerosols are key atmospheric constituents that significantly influence radiative transfer processes, cloud formation mechanisms, and atmospheric environmental dynamics (Dubovik et al., 2000; Levy et al., 2007a; Satheesh et al., 2005). Accurate aerosol parameter retrieval therefore plays a fundamental role in atmospheric remote sensing and directly governs AC performance (Zhang et al., 2009).

Numerous aerosol optical depth (AOD) retrieval algorithms have been developed to support aerosol characterization and AC applications. Physically based approaches remain the most widely adopted, with representative methods including the Dense Dark Vegetation algorithm (Kaufman et al., 1997) and the Deep Blue algorithm (Hsu et al., 2013). In recent years, multi-angle and multi-sensor retrieval strategies have further improved AOD estimation by enhancing surface–atmosphere separation and reducing uncertainties in SR assumptions. For example, the Multi-angle Implementation of Atmospheric Correction (MAIAC) algorithm developed for MODIS (Lyapustin et al., 2018) and MISR multi-angle retrievals combining nine viewing geometries have demonstrated improved performance, particularly over bright and heterogeneous surfaces (Chen et al., 2024).

Data-driven approaches, such as random forest, XGBoost, and deep neural networks, have also shown promising performance in capturing nonlinear relationships between atmospheric parameters and spectral observations (Radosavljevic et al., 2007). Recent studies have further incorporated temporal and spectral dependencies through advanced architectures, such as Transformer-based models applied to Himawari-8 time series data (She et al., 2024) and multilayer aerosol retrieval integrating geostationary SEVIRI data with CALIOP vertical aerosol profiles (Pashayi et al., 2025). Despite these advances, data-driven and multi-sensor methods generally require extensive training datasets and complex model structures, and they often lack physical interpretability. Consequently, physically based algorithms remain the dominant approach in operational AC systems and serve as a standard reference for remote sensing applications.

Within physically based AC frameworks, aerosol-type classification provides an efficient strategy to represent aerosol optical properties and improve retrieval adaptability. The development of aerosol classification has been greatly supported by globally distributed ground-based observation networks, including the Aerosol Robotic Network (AERONET) (Holben et al., 1998), the Sun–sky radiometer Observation Network (Li et al., 2018), and SKYNET (Takamura et al., 2004). Early aerosol studies introduced simplified physical models with fixed parameters describing particle size distribution, chemical composition, and optical characteristics such as extinction coefficient, single scattering albedo, and phase function. Representative developments include lower-layer aerosol classifications proposed by Shettle et al. (1979), naval aerosol characterization by Gathman et al. (1983), and desert aerosol models summarized by Longtin et al. (1988). Additionally, the World Meteorological Organization identified representative aerosol categories including continental, maritime, urban, desert, biomass burning, and stratospheric aerosols in its reports (World Meteorological Organization, 1983; World Meteorological Organization, 1986).

These fixed-parameter aerosol models remain essential components in radiative transfer models (RTMs), ensuring computational efficiency and stable performance. For instance, the MODTRAN model includes predefined aerosol types such as rural, urban, maritime, and desert (Berk et al., 2018), while the 6S and vector 6SV models incorporate continental, urban, maritime, and desert aerosol models (Vermote et al., 1997). These classical aerosol representations have been widely applied in AC processing across diverse environmental conditions.

However, fixed-parameter aerosol models may have limited adaptability under spatially and temporally varying aerosol conditions because they cannot fully capture the dynamic variability of atmospheric aerosols. To address this limitation, dynamic aerosol models, whose optical properties vary with AOD, have been developed based on global observational datasets. Since the 1990s, this research field has progressed significantly. Kaufman and Remer introduced fine-mode-dominated aerosol models such as urban/industrial and biomass burning/developing world aerosol types (Kaufman et al., 1997; Remer et al., 1998), while Ichoku et al. (2003) proposed highly absorbing aerosol models derived from African field observations (ECK et al., 2003). The integration of dynamic aerosol models provides more flexible and realistic atmospheric characterization and improves the adaptability of AC algorithms under diverse atmospheric conditions.

Through the integration of multiple aerosol models, AC algorithms have been continuously refined. Currently, fixed-parameter aerosol types remain dominant in operational AC processing. Commercial remote sensing software packages such as ATCOR (Richter et al., 2019), Atmospheric Correction Now (ACORN) (Miller et al., 2002), and Fast Line-of-sight Atmospheric Analysis of Hypercubes(FLAASH) (Anderson et al., 1999) rely on predefined aerosol types derived from MODTRAN to ensure efficient processing and reliable correction performance. Similarly, the Sentinel-2 AC processor Sen2Cor adopts a fixed atmospheric model and supports four predefined aerosol types based on the libRadtran4 database (Anderson et al., 2012; Mueller-Wilm et al., 2017). Their continued application reflects a balance between physical reliability and computational efficiency, making them suitable for large-scale routine remote sensing applications.

Meanwhile, dynamic aerosol models have been increasingly incorporated into satellite AC algorithms. A representative example is the evolution of Landsat AC processing, which transitioned from fixed aerosol assumptions to dynamic aerosol modeling. The LEDAPS algorithm (Vermote et al., 2007) applied to Landsat TM/ETM+ sensors adopts a fixed continental aerosol type, whereas the Land Surface Reflectance Code (LaSRC) algorithm for Landsat 8 integrates the Urban Clean dynamic aerosol model (Dubovik et al., 2002; Maciel et al., 2023; Vermote et al., 2016). Similarly, MODIS AC algorithms employ dynamic combinations of coarse-mode dust and fine-mode aerosol components (Kaufman et al., 1997; Remer et al., 2005), and later incorporated highly absorbing aerosol types to better represent global atmospheric variability (Ichoku et al., 2003; Remer et al., 2005). With the accumulation of global AERONET observations, generalized dynamic aerosol models have been developed to further improve MODIS aerosol products. Currently, aerosol information is available from two major MODIS aerosol retrieval algorithms: the MODIS Level-2 aerosol optical depth product (MOD04/MYD04) (Levy et al., 2007a; Levy et al., 2007b) and the MODIS atmospherically corrected SR product (MOD09/MYD09) (Dubovik et al., 2002; Lyapustin et al., 2021; Vermote et al., 2006b; Vermote et al., 2008), which employ distinct dynamic aerosol modeling schemes proposed by Levy et al. and Dubovik et al., respectively. These aerosol products have been widely utilized in operational applications, including NASA's Web-enabled Landsat Data project for improving Landsat 7 SR data and the AC of land observations acquired by the VIIRS sensor onboard the NPP satellite (Roy et al., 2010; Superczynski et al., 2017). Overall, while fixed aerosol models remain widely adopted due to their stability and ease of implementation, dynamic aerosol models provide improved adaptability under complex atmospheric conditions.

However, despite the widespread operational use of dynamic aerosol models, their performance has not been comprehensively evaluated under a consistent AC framework. Existing studies indicate that the use of different aerosol representations may introduce inconsistencies in AOD retrieval (Grey et al., 2006), which can subsequently propagate into SR uncertainties. In practice, although major aerosol and AC products, such as MOD04, MOD09, and the LaSRC algorithm, all adopt dynamic aerosol types, they employ different subtype libraries and subtype-selection strategies. This discrepancy may lead to variations in aerosol optical properties used in AC, whereas systematic inter-comparisons among these types remain limited. Therefore, a comparative assessment of widely used dynamic aerosol types is essential for improving retrieval accuracy and optimizing aerosol type selection (Zhang et al., 2022).

Additionally, existing validations of dynamic aerosol-related products are still insufficient. Among these products, the Landsat 8 SR product generated by the LaSRC algorithm—one of the most widely used dynamic aerosol-related SR datasets—is a key dataset for operational applications. However, previous validation studies have reported systematic deviations over high-reflectance surfaces such as desert playas, where SR tends to be underestimated, particularly in short-wavelength visible (VIS) bands including coastal aerosol and blue bands (Mann et al., 2024; Meghraj et al., 2023). Moreover, product documentation and independent validation studies indicate that SR retrieval uncertainties increase under challenging atmospheric or illumination conditions, with larger errors frequently observed in shorter VIS wavelengths (Roy et al., 2014; Vermote et al., 2016). Despite these potential uncertainties, current evaluations of dynamic aerosol-related products remain limited in scope, with existing validation efforts constrained by narrow site coverage, restricted reflectance ranges, and insufficient land-cover-specific assessments. For example, Vermote et al. (2006b) validated the LaSRC algorithm using only 33 sites, with SR evaluation in VIS bands primarily confined to low-reflectance conditions, which hampers a comprehensive understanding and effective use of the product.

The above limitations highlight that current evaluations of dynamic aerosol types are still incomplete. In particular, systematic inter-comparisons between different types remain lacking, and existing studies are restricted in terms of site coverage, reflectance range, spectral bands, and land-cover-specific validation. These limitations underscore the need for a systematic comparison of dynamic aerosol types to comprehensively assess their performance under diverse conditions.

To address these gaps, this study focuses on three representative dynamic aerosol types: the MOD04-based type, the MOD09-based type, and the LaSRC Urban Clean type. The MOD04-based and MOD09-based types denote dynamic aerosol types constructed according to the aerosol subtype definitions and parameterization strategies used in the MOD04 and MOD09 aerosol retrieval frameworks, respectively. Urban Clean is one of the MOD09 aerosol subtypes and is used as the aerosol model in the operational LaSRC algorithm. All three types are dynamic because their aerosol size parameters (radius, standard deviation, volume distribution) and complex refractive index vary with AOD. However, they differ in their aerosol subtype libraries and subtype-selection strategies. The MOD04-based type includes four aerosol subtypes selected according to location and season, whereas the MOD09-based type includes five aerosol subtypes selected according to the minimum aerosol retrieval error. Therefore, comparing these three types provides a basis for assessing how different dynamic aerosol subtype libraries and subtype-selection strategies influence AOD and SR retrievals in Landsat 8 AC.

This study presents a comprehensive evaluation of these three dynamic aerosol types on Landsat 8 AC performance, based on multisite observations from global AERONET sites collected throughout 2022. To quantify their impact on retrieval performance, AOD accuracy is evaluated for all three types, and significance analyses are performed to assess the robustness of the results. SR retrieval performance is further assessed for four SR products—including the SR products corresponding to three aerosol types and the LaSRC SR product—by examining overall and per-band reflectance, variations across the full 0–1 reflectance range, and differences across land-cover types, providing a comprehensive evaluation under diverse conditions. By providing a systematic comparison of widely used dynamic aerosol types, this study offers guidance for selecting appropriate aerosol types in operational AC and informs the development of more flexible, task-specific strategies, thereby improving AC performance in operational remote sensing applications.

2 Data sources and characteristics

2.1 Landsat 8 dataset

Landsat 8 satellite data were selected as the primary data source to satisfy the stability and temporal continuity requirements of quantitative analysis. To support validation over diverse environmental conditions, 100 globally distributed AERONET sites (Holben et al.,1998) were systematically selected to produce a validation-referenced SR series spanning the entire year 2022. The geographical distribution of these sites is shown in Fig. 1, overlaid on global climate zones. The sites span 12 major climate zones, with the largest numbers located in humid cold temperate (Df, 26 sites) and humid warm temperate (Cf, 26 sites) regions, followed by warm summer-dry (Cs, 10 sites), steppe (Bs, 8 sites), desert (Bw, 8 sites), tropical savanna (Aw, 7 sites), warm winter-dry (Cw, 5 sites), subarctic continental (Ds, 4 sites), tropical rainforest (Af, 4 sites), subarctic monsoon (Dw, 1 site), and ice-cap (ET, 1 site) climates. The number of sites by continent is summarized in Table 1, further illustrating the global coverage of the dataset. Together, the climatic and continental distributions demonstrate that the selected sites provide broad spatial and environmental representativeness, offering a diverse basis for evaluating the performance of dynamic aerosol types.

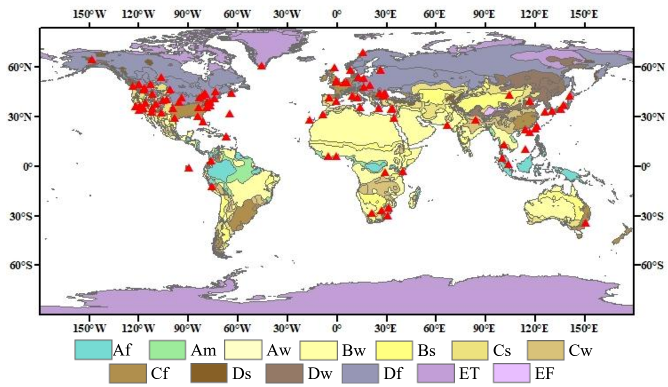

Figure 1: The selected 100 AERONET sites distributed worldwide.

Table 1. Number of AERONET sites used by continent (N = 100).

Continent	Number of Sites
Africa	9
Asia	20
Europe	24
Oceania	1
North America	43
South America	3

Launched on February 11, 2013, as the eighth satellite in the US Landsat program, Landsat 8 carries two key sensors: an Operational Land Imager (OLI) and a Thermal Infrared Sensor (TIRS). Landsat 8 has 11 spectral bands, including nine multispectral OLI bands covering the VIS to shortwave infrared (SWIR) spectrum (433-2300 nm) and two TIRS thermal infrared bands (10.6-12.51 μm) designed for land surface temperature and moisture monitoring through terrestrial thermal radiation measurements (Roy et al., 2014).

This study utilized the first seven bands of both Landsat 8 Tier 1 Level 1 and Level 2 products with high-quality radiometric correction and orthorectification (Dwyer et al., 2018). Detailed band information is provided in Table 2. In total, more than 3,800 Landsat 8 scenes were identified at the selected 100 AERONET sites for the year 2022. After rigorous spatiotemporal matching and quality screening, 634 scenes were retained as the final dataset (Fig. 2). Specifically, AERONET measurements were matched with Landsat 8 images within ±15 min of the satellite overpass time. For each site, Landsat scenes were cropped to a 6 × 6 km window centered on the AERONET location to ensure spatial homogeneity, which is finer than the 9 × 9 km window commonly used in previous validation studies (Doxani et al., 2023). Cloud and cloud-shadow pixels were identified using the LaSRC QA band (CFMask), a widely used cloud masking algorithm for Landsat data that has been extensively validated with an overall accuracy of approximately 90% (Foga et al., 2017). Scenes with more than 20% cloud-contaminated pixels within the study window were excluded. All processing steps were implemented on the Google Earth Engine platform to ensure consistency and computational efficiency.

Table 2. Landsat 8 bands in the reflected solar spectraum.

	Band Range (μ m)	SNIR	SR (m)
Band1-COASTAL/AEROSOL	0.43-0.45	130	30
Band2-Blue	0.45-0.51	130	30
Band3-Green	0.53-0.59	100	30
Band4-Red	0.64-0.67	90	30
Band5-NIR	0.85-0.88	90	30
Band6-SWIR1	1.57-1.65	100	30
Band7-SWIR2	2.11-2.29	100	30

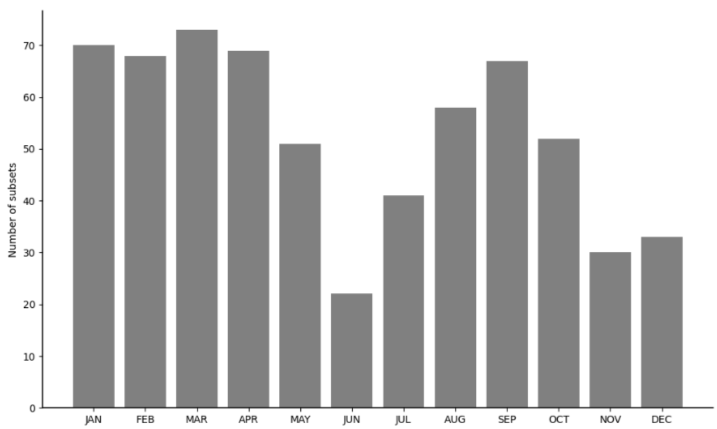

Figure 2: Monthly distribution of the 6 × 6 km Landsat 8 subsets across 100 AERONET sites (Fig. 1) for the year 2022.

Such a standardized processing strategy is required for the validation of atmospheric parameters (e.g., AOD) and SR retrieval to ensure the representation of AERONET measurements over a reasonable spatial extent.

2.2 AOD reference dataset

AERONET (Holben et al.,1998) is a fundamental ground-based observation network in atmospheric sciences that provides globally distributed, high-precision, and high-temporal-resolution aerosol optical parameters. It provides AODs in multiple spectral bands of automated sun photometers, enabling the interpolation of AOD at 550 nm (AOD_{550}), a wavelength commonly used as a key indicator to assess the aerosol concentration and distribution in the atmosphere.

Level-2 AOD data for 2022 were used because of their high quality, ensuring higher precision (with an uncertainty of 0.01–0.02) and stability with cloud screening and instrument calibration (Giles et al., 2019), making them well-suited for AOD comparison studies. To ensure temporal consistency between Landsat 8 imagery and AERONET observations and broader validation coverage across diverse regions, AOD retrievals were selected within ±15 min of Landsat 8 overpass time. The AOD_{550} was then interpolated using measurements at two adjacent wavelengths (440 and 675 nm) by assuming the Junge distribution, as shown in Eq. (1–3):

$$\tau(0.55) = \beta * 0.55^{-\alpha} , \tag{1}$$

$$\alpha = -\frac{\ln \frac{\tau(\lambda_1)}{\tau(\lambda_2)}}{\ln \frac{\lambda_1}{\lambda_2}} , \tag{2}$$

$$\beta = \frac{\tau(\lambda_1)}{\lambda_1^{-\alpha}} = \frac{\tau(\lambda_2)}{\lambda_2^{-\alpha}} . \tag{3}$$

where, $\tau(\lambda_1)$, $\tau(\lambda_2)$ represents the AOD at 440 nm and 675 nm, while α and β denote the Ångström exponent (Ångström, 1964) and the turbidity coefficient, respectively.

2.3 SR reference dataset

Common sources of reference data for satellite SR retrieval validation include in-situ ground spectral measurements, other SR products with high accuracy, and AERONET-based SR associated with an accurately validated radiative transfer code. While the first source seems to be direct validation data, it lacks systematic measurements with adequate spatial and spectral resolutions. Instead, indirect validation using the latter two reference sources has been used extensively for SR product comparison (Vermote et al., 2016). In practice, MODIS SR is used as a reference dataset owing to its well-established reliability. However, the spectral and spatial differences between MODIS and Landsat 8 introduce additional errors. Therefore, the AERONET-based SR using the vector 6S 4.1 (Vermote et al., 1997) code (hereafter referred to as 6SV), accounting for the polarization effect with a mean relative accuracy of 0.4–0.6% (Vermote et al., 2006a), was adopted as the 'true' to validate other Landsat SR retrieved by different approaches.

The critical input parameters for 6SV to compute the SR of Landsat 8 scenes included: 1) spectral response functions (SRF) of Landsat 8 OLI; 2) elevations for AERONET sites; 3) atmospheric models (e.g., mid-latitude summer/winter) estimated based on data acquisition dates and site locations; 4) aerosol properties, including aerosol particle size distribution from AERONET Level 2.0 inversion products, and AOD550 interpolated from AERONET spectral AOD retrievals; 5) geometric imaging parameters, including solar zenith, solar azimuth, viewing zenith, and viewing azimuth; and 6) image acquisition date and time.

3 Methodology

3.1 AC method

This section delineates the AC methodology, focusing on five key aspects: radiative transfer principles, look-up table (LUT) construction, aerosol-type selection, AOD retrieval, and other auxiliary parameter acquisition. To comprehensively evaluate the advantages and limitations of different aerosol types on AC, three dynamic aerosol types (MOD04-based, MOD09-based, and Urban Clean) were used for Landsat 8 AC to retrieve AOD and SR.

1) **AC principle**

The solar radiation received by the sensor consists of both surface-reflected and atmospheric-scattered components. Assuming a Lambertian surface and considering atmospheric absorption and scattering, these contributions can be reformulated in terms of the top-of-atmosphere (TOA) reflectance. For narrow spectral bands outside the major water vapor absorption features, TOA reflectance can be calculated as follows (Vermote et al., 2008):

$$\rho^*(\theta_s,\theta_v,\varphi,P,Aer,U_{H_2O},U_{O_3}) = T_{g_{OG}}(m,P)T_{g_{O_3}}(m,U_{O_3})\cdot[\rho_{atm}(\theta_s,\theta_v,\varphi,P,Aer,U_{H_2O}) + Tr_{atm}(\theta_s,\theta_v,P,Aer)\frac{\rho_t}{1-S_{atm}(P,Aer)\cdot\rho_t}T_{g_{H_2O}}(m,U_{H_2O})], \quad (4)$$

where $\rho^*(\theta_s,\theta_v,\varphi,P,Aer,U_{H_2O},U_{O_3})$ represents the TOA reflectance, θ_s represents the solar zenith angle, θ_v represents the view zenith angle, and φ represents the relative azimuth angle. P is the atmospheric pressure, and Aer describes aerosol properties, including AOD, aerosol single-scattering albedo, and phase function. where U_{H_2O} and U_{O_3} represent the water vapor content (WVC) and ozone content, respectively. Additionally, $T_{g_{H_2O}}$, $T_{g_{O_3}}$, and $T_{g_{OG}}$ are the gaseous transmissions of water vapor, ozone, and other gases, respectively; where $\rho_{atm}(\theta_s,\theta_v,\varphi,P,Aer,U_{H_2O})$ denotes the atmospheric intrinsic reflectance, $Tr_{atm}(\theta_s,\theta_v,P,Aer)$ represents the total atmospheric transmittance, and ρ_t represents the SR retrieved by the AC procedure, and $S_{atm}(P,Aer)$ represents the atmospheric spherical albedo.

To simplify the computational processes in Eq. (4), we employ the approach used by Vermote et al. (2006b) for MODIS. This method separately addresses the atmospheric absorption and scattering effects, thereby considerably reducing the complexity and storage requirements for LUT construction. The first step involved correcting the TOA reflectance (hereafter referred to as the corrected TOA reflectance) for absorption effects, including adjustments for general gas absorption (excluding water vapor and ozone), ozone absorption, and water vapor. The corrected TOA reflectance can be expressed as follows:

$$\rho_c^*(i) = \frac{1}{T^i_{g_{OG}}(m,P)\cdot T^i_{g_{O_3}}(m,U_{O_3})\cdot T^i_{g_{H_2O}}(m,U_{H_2O})}\rho^*(i), \quad (5)$$

$$T^i_{g_{OG}}(m,P) = \exp[m(a_0^iP + a_1^i\ln(P)) + \ln(m)(b_0^iP + b_1^i\ln(P)) + m\ln(m)(c_0^iP + c_1^i\ln(P))], \quad (6)$$

$$T^i_{g_{O_3}}(m,U_{O_3}) = \exp(-ma^i_{O_3}U_{O_3}), \quad (7)$$

$$T^{i}_{g_{H_2O}}(m,U_{H_2O}) = \exp[a^{i}_{H_2O} m U_{H_2O} + b^{i}_{H_2O} \ln(m U_{H_2O}) + c^{i}_{H_2O} m U_{H_2O} \ln(m U_{H_2O})], \tag{8}$$

$$m = \frac{1}{\cos(\theta_s)} + \frac{1}{\cos(\theta_v)}, \tag{9}$$

where i is the Landsat 8 band number, m is the relative atmospheric air mass, and P is atmospheric pressure (atm). The parameters a^{i}_{0}, a^{i}_{1}, b^{i}_{0}, b^{i}_{1}, c^{i}_{0}, c^{i}_{1}, $a^{i}_{O_3}$, $a^{i}_{H_2O}$, $b^{i}_{H_2O}$, and $c^{i}_{H_2O}$ are associated with the SRFs of Landsat 8. The parameters for the different Landsat 8 bands were retrieved by running the 6SV code under different atmospheric conditions. The corrected TOA reflectance is expressed as follows:

$$\rho^{*}_{c}(\theta_s,\theta_v,\varphi,P,Aer,U_{H_2O},U_{O_3}) = \frac{\rho_{atm}(\theta_s,\theta_v,\varphi,P,Aer,U_{H_2O})}{T_{g_{H_2O}}(m,U_{H_2O})} + Tr_{atm}(\theta_s,\theta_v,P,Aer)\frac{\rho_t}{1-S_{atm}(P,Aer)\cdot\rho_t}, \tag{10}$$

A further approximation allows unknown atmospheric parameters (ρ_{atm}, Tr_{atm}, S_{atm}) to be computed only at standard pressure, leading to an additional reduction in LUT size. The relevant formulas are as follows:

$$\rho_{atm}(\theta_s,\theta_v,\varphi,P,Aer,U_{H_2O}) = \rho_R(\theta_s,\theta_v,\varphi,P) + \left[\rho_{R+Aer}(\theta_s,\theta_v,\varphi,P_0,Aer) - \rho_R(\theta_s,\theta_v,\varphi,P_0)\right]\cdot T_{g_{H_2O}}(m,\frac{U_{H_2O}}{2}), \tag{11}$$

$$\rho_R(\theta_s,\theta_v,\varphi,\tau_R(P)) = \rho_R(\theta_s,\theta_v,\varphi,\tau_R\cdot P/P_0), \tag{12}$$

$$Tr_{atm}(\theta_s,\theta_v,P,Aer) = T_{atm}(\theta_s,P,Aer)T_{atm}(\theta_v,P,Aer), \tag{13}$$

$$T_{atm}(\theta,P,Aer) = T_{atm}(\theta,P_0,Aer)\frac{T_R(\theta,P)}{T_R(\theta,P_0)}, \tag{14}$$

$$S_{atm}(P,Aer) = \left(S_{atm}(P_0,Aer) - S_R(P_0)\right) + S_R(P), \tag{15}$$

$$S_R(P) = \frac{1}{4+3P/P_0\cdot\tau_R}\left[3P/P_0\cdot\tau_R - 4E_3(P/P_0\cdot\tau_R) + 6E_4(P/P_0\cdot\tau_R)\right]. \tag{16}$$

where ρ_{R+Aer} represents the aerosol and Rayleigh scattering effects, and τ_R is the Rayleigh optical thickness. T_R represents the atmosphere transmission function due to molecular scattering, T_{atm} is the upwelling or downwelling atmospheric transmittance, and S_R is the Rayleigh spherical albedo. And E_3, E_4 are exponential integral function.

Through the two-step simplification, the AC process ultimately requires only a limited set of unknown atmospheric parameters, including τ_R, ρ_{R+Aer}, T_{atm}, S_{atm} at standard atmospheric pressure, AOD, WVC, ozone content, and atmospheric pressure P. The following section provides a detailed description of the unknown parameters.

2) **LUT construction**

In the remote sensing domain of AC and atmospheric parameter retrieval, RTMs account for multiple complex atmospheric radiation processes that require large amounts of computation. However, it is impossible to run RTMs directly for large-scale image processing owing to their high time costs. Therefore, the LUT technique is typically used for this purpose. LUTs precompute and store RTM-based results under various conditions, enabling rapid retrieval of atmospheric parameters through interpolation between discrete nodes. This approach substantially reduces redundant computations and enhances the processing efficiency. LUT-based methods are widely used in remote sensing, and numerous AC software packages, such as ISDAS (Staenz et al., 1997; Staenz et al., 1998), ATCOR (Schläpfer et al., 2002; Brazile et al., 2008; Perkins et al., 2012a; Perkins et al., 2012b), Atmospheric Removal Program (ATREM) (Gao et al., 1992), MODIS product processing system (Toller et al., 2009), and LEDAPS (Masek et a., 2006), utilize RTMs (e.g., MODTRAN or 6S) to pre-construct LUTs to accelerate the processing procedures.

In this study, a dynamic aerosol-type LUT was constructed using the 6SV code to enable the efficient interpolation of AC parameters under varying aerosol conditions, offering greater adaptability compared to conventional fixed-type LUTs. To accommodate the diverse atmospheric and geometric configurations encountered in real-world scenes, the LUT includes six input parameter dimensions (Table 3): viewing zenith angle (VZ), solar zenith angle (SZ), relative azimuth angle (RAA), aerosol type (AerT), 550 nm AOD (AOD550), and spectral band (Band). For each parameter combination, the LUT outputs the corresponding atmospheric radiative parameters, assuming a standard atmospheric pressure. The column WVC and total column ozone amount were fixed at 1.0 $g\cdot cm^{-2}$ and 300 DU, respectively, as their spatial and temporal variations exert only minor influences on the TOA. Accounting for these variables would considerably increase the computational and storage requirements without substantially improving accuracy (Guanter et al., 2009). Consequently, the six selected parameters were considered sufficient to characterize the atmospheric conditions pertinent to this study.

Table 3. LUT variables settings.

Variables	Setting
VZ	0,12,24,36
SZ	1.5,12,24,36,48,54,60,66,72
RAA	0,30,60,90,120,150,180
Aerosol Type	MOD04-based: Strongly Absorbing, Moderately Absorbing, Weakly Absorbing, Spheroid/Dust
(AerT)	MOD09-based: Urban Clean, Urban Polluted, Smoke Low Absorption, Smoke High Absorption, Dust
AOD_{550}	0.01,0.05,0.1,0.15,0.2,0.3,0.4,0.6,0.8,1,1.2,1.4,1.6,1.8,2,2.3,2.6,3,3.5,4,4.5,5.0
Band	1、2、3、4、5、6、7

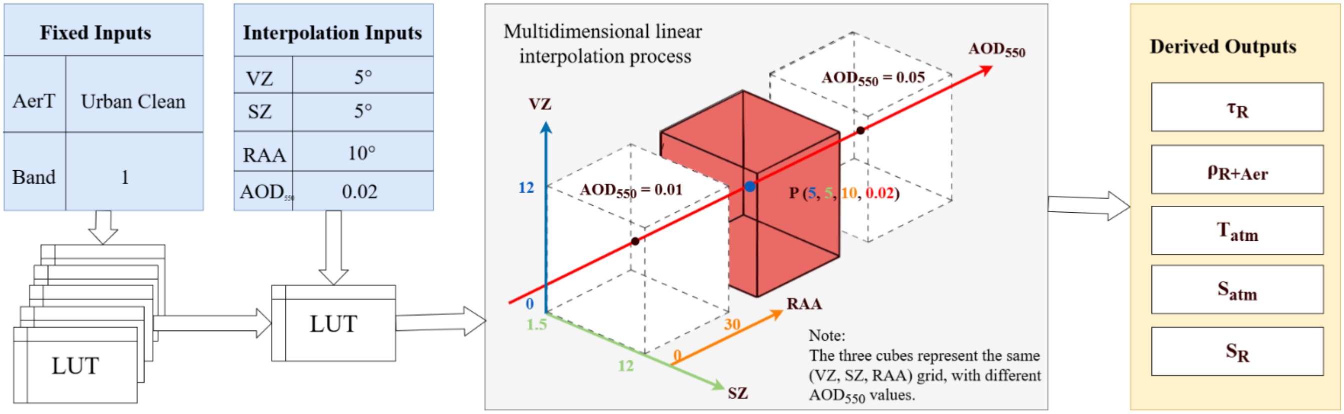

Figure 3: Input–Output Framework for Atmospheric Radiative Transfer Calculations Using Multidimensional LUT.

In total, 349,272 valid parameter combinations were generated for the six variables. Each combination was systematically computed using 6SV code, compiled into an LUT, and converted into a binary format to reduce the storage footprint. Fig. 3 demonstrates the multidimensional linear interpolation process for retrieving AC parameters when AerT = Urban Clean, Band = 1, VZ = 5°, SZ = 5°, RAA = 10°, and AOD_{550} = 0.02. First, the appropriate sub-LUT is selected according to the specified aerosol type (AerT) and spectral band (Band). Then, for a given observation geometry (VZ, SZ, RAA) and aerosol AOD (AOD_{550}), the required parameters are obtained through multidimensional linear interpolation among the nearest neighboring nodes in the LUT. The interpolated results provide the AC parameters (τ_R, ρ_{R+Aer}, T_{atm}, S_{atm}, S_R) required for SR retrieval.

3) **Dynamic aerosol type selection**

This study incorporated three representative dynamic aerosol types: MOD04-based, MOD09-based, and Urban Clean, all of which were derived from global AERONET results. Specifically, aerosol-subtype selection for MOD04-based adheres to seasonal and regional characteristics, whereas MOD09-based aerosol subtypes are optimized using error minimization criteria. Urban Clean, operating as an aerosol subtype under MOD09-based conditions, remained fixed during the AC in terms of type selection. All three types were parameterized using a bi-lognormal distribution model, with their coefficients dynamically adjusted in response to AOD variations.

a) MOD04-based types

MOD04-based aerosol types employ a fixed classification scheme based on 1°×1° global grid cells, with variations governed by seasonal and regional aerosol distribution patterns. This aerosol-subtype distribution was statistically derived from multiyear AERONET observational datasets, encompassing three fine-mode-dominant subtypes (strongly, moderately, and weakly absorbing) and one coarse-mode-dominant subtype (spheroid/dust). The optical parameters for the four subtypes were adopted from Levy et al. (2007). As illustrated in Fig. 4, the quarterly spatial distributions of the three fine-mode and one coarse-mode aerosol subtype were adapted from the methodologies of Levy et al. (2003) and Friedl et al. (2002). .

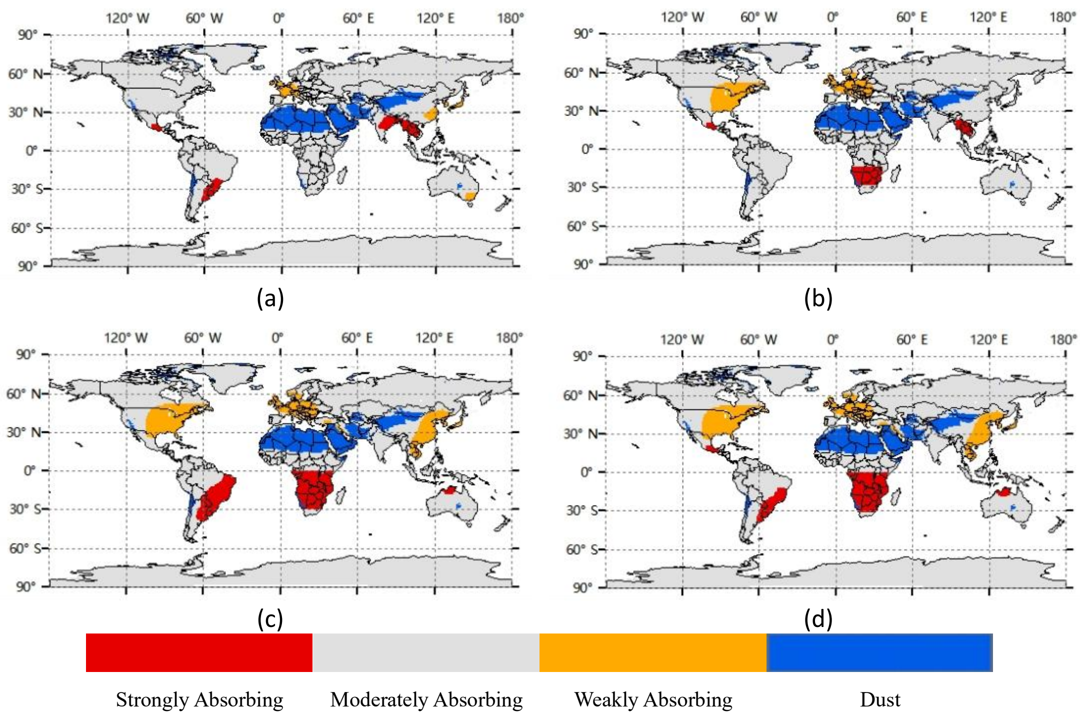

Figure 4: 1°*1°Global land surface aerosol types across different seasons. (a) December, January and February (DJF)； (b) March, April and May (MAM)； (c)June, July and August (JJA); (d) September, October and November (SON).

b) MOD09-based types

MOD09-based type was statistically derived from eight years of AERONET observational datasets and comprised four subtypes: urban clean, urban polluted, smoke low-absorption, and smoke high-absorption (Remer et al., 2005). Each type was parameterized dynamically using AOD-dependent coefficients. During operational implementation, an additional dust aerosol type (Remer et al., 1998) was incorporated to improve the environmental representativeness and accuracy of AC. For AOD retrieval for a given pixel, the goodness-of-fit residuals for all five candidate subtypes were computed and compared. Subsequently, the type exhibiting the minimum residual is selected for inversion to ensure optimal retrieval accuracy via adaptive model selection.

$$AOD_{MOD09-based} = \arg\min\left(\Delta_{UrbanClean}, \Delta_{UrbanPolluted}, \Delta_{SmokeLow}, \Delta_{SmokeHigh}, \Delta_{Dust}\right), \quad (17)$$

c) Urban Clean

The Urban Clean aerosol type, designated in the official Landsat 8 official AC algorithm (LaSRC), has optical parameters that are dynamically adjusted according to AOD variations (Remer et al., 2005).

4) **AOD retrieval**

The AOD retrieval framework employs MODIS-derived band ratio relationships and Landsat 8-9 ratio files (Vermote et al., 2016) for computational optimization. First, the ratio file generates spectral indices between the deep blue (DB), blue (B), SWIR, and red (R) bands. The $NDVI_{SWIR}$ index substitutes the red band in the Normalized Difference Vegetation Index (NDVI) formula with the SWIR band, maintaining numerical proximity while reducing the sensitivity to aerosols. This parameterization of the ratio as a function of $NDVI_{SWIR}$ enabled the capture of its potential seasonal and interannual variability.

Subsequently, iterative optimization was performed, where residuals were calculated based on band ratio relationships. The AOD value corresponding to the minimum residual was identified through cyclic computation, and subsequently refined using quadratic fitting.

$$Ratio = a * NDVI_{SWIR} + b \quad , \tag{18}$$

$$NDVI_{SWIR} = \frac{\rho_t(b_5) - \rho_t(b_7)/2}{\rho_t(b_5) + \rho_t(b_7)/2} \quad , \tag{19}$$

$$\Delta = \sqrt{\left(\rho_t(b_1) - Ratio1 \cdot \rho_t(b_4)\right)^2 + \left(\rho_t(b_2) - Ratio2 \cdot \rho_t(b_4)\right)^2 + \left(\rho_t(b_7) - Ratio7 \cdot \rho_t(b_4)\right)^2} \quad , \tag{20}$$

where a and b denote the band ratio values, and $\rho_t(b_1)$, $\rho_t(b_2)$, $\rho_t(b_4)$, $\rho_t(b_5)$, and $\rho_t(b_7)$ represent the SR in the deep blue, blue, red, near-infrared, and shortwave infrared bands, respectively.

5) **Auxiliary parameter acquisition**

Atmospheric Pressure: In AC processes, parameters such as path radiance and total atmospheric transmittance are inherently influenced by atmospheric pressure. Consequently, accurate SR retrieval requires a reliable pressure data source. In this study, the atmospheric pressure was estimated based on an empirical relationship with elevation derived from a Digital Elevation Model (DEM). In particular, for each DEM pixel with elevation H (km), the corresponding atmospheric pressure P (atm) was calculated as

$$P = 1013 \cdot \exp(-H/8) \quad , \tag{21}$$

WVC: The WVC used in this study was obtained from the National Centers for Environmental Prediction and the National Center for Atmospheric Research Reanalysis dataset developed by the NCEP/NCAR. This global reanalysis product, available since 1948, provides the WVC (kg/m³) with a temporal resolution of 6 h and a spatial resolution of 2.5° × 2.5°. The data were spatially interpolated to image site locations and temporally aligned with the corresponding acquisition time.

Ozone: Ozone data were derived from the Ozone Monitoring Instrument onboard NASA's Aura satellite, which provides daily global ozone column densities in Dobson Units (DU) at a resolution of 2.5° × 2.5°. For each scene, site-specific ozone concentrations were extracted based on geographic location and image acquisition time.

The integration of these datasets enabled the accurate estimation of atmospheric pressure, WVC, and ozone, which are the three essential inputs for the AC process, thereby enhancing the accuracy of AOD and SR retrievals.

3.2 Accuracy validation method

The accuracy of AOD retrieval was assessed using scatter plots, where the slope and correlation coefficient from the linear regression characterized the agreement between the retrieved and ground truth values. In addition, the RMSE, coefficient of determination (R^2) and Bias were computed to quantify retrieval performance across different aerosol types. These statistical metrics provide an objective basis for evaluating the algorithm performance. The corresponding formulas are as follows:

$$Bias = \frac{1}{n}\sum_{i=1}^{n}\left(AOD_{model} - AOD_{ground}\right), \tag{22}$$

$$RMSE = \sqrt{\frac{1}{n}\sum_{i=1}^{n}\left(AOD_{model} - AOD_{ground}\right)^2}, \tag{23}$$

$$R^2 = 1 - \frac{\sum_{i=1}^{n}\left(AOD_{model} - AOD_{ground}\right)^2}{\sum_{i=1}^{n}\left(AOD_{ground} - \overline{AOD_{ground}}\right)^2}, \tag{24}$$

where AOD_{model}, AOD_{ground} denotes the model-retrieved and ground-truth AOD values, and n represents the total number of image samples. We computed 95% confidence intervals (CIs) for all parameters via bootstrapping (1,000 iterations). Additionally, R^2 values were calculated for both the linear regression fit (R^2_linear) and aerosol-type-specific predictions (R^2_AerT).

Pairwise statistical significance of RMSE and Bias differences between aerosol types was assessed using paired permutation tests, with Holm-adjusted p-values to control the family-wise error rate. R^2_AerT differences were evaluated using Paired bootstrap resampling of ΔR^2_AerT, followed by Holm adjustment. Statistical significance was determined at $\alpha = 0.05$, and results are reported with significance stars (*** $p < 0.001$, ** $p < 0.01$, * $p < 0.05$, ns: not significant).

2) **SR accuracy validation**

To validate the SR, we employed a three-tiered evaluation framework encompassing the overall, per-band, and reflectance-range levels. The assessment is based on three key metrics: accuracy (A), precision (P), and uncertainty (U). These indicators enable a comprehensive evaluation of reflectance performance under varying aerosol types, identifying the errors and uncertainties introduced by each. Specifically, A reflects the agreement between the retrieved and reference values, P indicates result consistency, and U captures the potential error range during the measurement process. The relevant formulas are as follows (Vermote et al., 2016).

$$A = \frac{1}{n}\sum_{i=1}^{n}\left(\rho_i^e - \rho_i^t\right), \tag{25}$$

$$P = \sqrt{\frac{1}{n-1} \times \sum_{i=1}^{n}\left(\varepsilon_i - A\right)^2}, \tag{26}$$

$$U=\sqrt{\frac{1}{n}\times\sum_{i=1}^{n}\varepsilon_i^{\,2}}\,, \tag{27}$$

Where ρ_i^e refers to the computed value, ρ_i^t represents the true value, n indicates the number of calculations, and ε_i denotes the difference between the computed value and the true value. All metrics were accompanied by 95% CIs constructed via bootstrapping (n=1,000).

In addition to the comprehensive accuracy validation described above, we conducted a targeted analysis focusing on five representative land-cover types (building, snow, soil, vegetation, water). For each land-cover category, the corresponding pixels were extracted using commonly-used remote sensing ecological index (RSEI), including the Normalized Difference Building Index (Zha et al., 2003), the Normalized Difference Snow Index (Hall et al., 2011), the Bare Soil Index (Rikimaru et al., 2002), NDVI (Rouse et al., 1974) and the Normalized Difference Water Index (McFeeters et al., 1996). The corresponding formulas are as follows:

Building: $$NDBI=\frac{\rho_{\mathrm{t}}(b_6)-\rho_{\mathrm{t}}(b_5)}{\rho_{\mathrm{t}}(b_6)+\rho_{\mathrm{t}}(b_5)}>0\,, \tag{28}$$

Snow: $$NDSI=\frac{\rho_{\mathrm{t}}(b_3)-\rho_{\mathrm{t}}(b_6)}{\rho_{\mathrm{t}}(b_3)+\rho_{\mathrm{t}}(b_6)}>0.3\,, \tag{29}$$

Soil: $$BSI=\frac{\left(\rho_{\mathrm{t}}(b_6)+\rho_{\mathrm{t}}(b_4)\right)-\left(\rho_{\mathrm{t}}(b_5)+\rho_{\mathrm{t}}(b_1)\right)}{\left(\rho_{\mathrm{t}}(b_6)+\rho_{\mathrm{t}}(b_4)\right)+\left(\rho_{\mathrm{t}}(b_5)+\rho_{\mathrm{t}}(b_1)\right)}>0\,, \tag{30}$$

Vegetation: $$NDVI=\frac{\rho_{\mathrm{t}}(b_5)-\rho_{\mathrm{t}}(b_4)}{\rho_{\mathrm{t}}(b_5)+\rho_{\mathrm{t}}(b_4)}>0.1\,, \tag{31}$$

Water: $$NDWI=\frac{\rho_{\mathrm{t}}(b_3)-\rho_{\mathrm{t}}(b_5)}{\rho_{\mathrm{t}}(b_3)+\rho_{\mathrm{t}}(b_5)}>0.4\,. \tag{32}$$

where $\rho_{\mathrm{t}}(b_3)$ and $\rho_{\mathrm{t}}(b_6)$ represent the SR in the green and SWIR bands.

For each land-cover type, the SR retrieval performance across seven spectral bands was quantitatively evaluated using reference data. Statistical performance metrics, including RMSE, and Bias, were calculated to compare the accuracy of different SR products.

4 Results

4.1 AOD validation results

The scatter plot in Fig. 5, generated from 451 cloud-free images, illustrates the AOD retrieval performance at 550 nm for the MOD04-based, MOD09-based, and Urban Clean dynamic aerosol types. As no official Landsat 8 AOD products are currently available (She et al., 2022), the comparison is limited to these three aerosol types. The x-axis denotes the AERONET observations, and the y-axis shows the corresponding estimated AOD values. The black dashed line denotes the 1:1 reference, which serves as a benchmark for ideal agreement between the retrieved and ground-truth values. Flanking this line, the black solid lines delineate the empirical uncertainty envelope—defined as $0.15 \times AOD_{550} \pm 0.05$—based on the empirical uncertainty of MODIS land AOD retrievals (Remer et al., 2005). The solid blue line represents the least-squares regression fit, which highlights the relationship between the two datasets. To assess AOD retrieval accuracy, three statistical metrics, RMSE, bias, and coefficient of determination (R^2_AerT), were calculated (Table 4).

The results indicated noticeable differences among the scatter plots for the three dynamic aerosol types. In terms of scatter distribution, most MOD04-based data points fell within the uncertainty range (black solid lines) and were relatively concentrated. The Urban Clean type followed, displaying a relatively uniform distribution, but appearing slightly more dispersed than the MOD04-based type. In contrast, MOD09-based type exhibited the highest dispersion, with a significant proportion of points falling outside the uncertainty bounds, indicating a greater variability in the data.

Upon further examination of the regression lines, the slopes for the MOD04-based, MOD09-based, and Urban Clean types were 0.9047, 1.0852, and 1.0295, respectively. The Urban Clean regression line was the closest to the 1:1 reference line, suggesting an optimal fit. The MOD04-based regression line, with a slope of less than one, intersects the 1:1 line, indicating a degree of bias. By contrast, the MOD09-based regression line exhibited the greatest deviation from the 1:1 line, suggesting a less accurate fit.

According to the accuracy metrics in Table 4, the RMSE values ranged from 0.0437 to 0.0612, Bias values ranged from 0.0052 to 0.0264, and R^2_AerT values ranged from 0.4586 to 0.7236. Statistical significance was assessed using paired permutation tests for RMSE and Bias, and paired bootstrap resampling for ΔR^2_AerT, followed by Holm correction for multiple comparisons. The results in Table 5 indicate that RMSE and Bias differences between all type pairs were statistically significant ($p < 0.001$, ***), with MOD04-based significantly outperforming MOD09-based and Urban Clean, and Urban Clean outperforming MOD09-based. In contrast, although R^2_AerT differences showed consistent trends (MOD04-based > Urban Clean > MOD09-based), the bootstrap confidence intervals for ΔR^2_AerT overlapped zero in several comparisons, and none of the R^2_AerT differences reached statistical significance after multiple-comparison adjustment. These findings demonstrate that MOD04-based consistently provides the most accurate and least biased AOD estimates, while improvements in goodness-of-fit over other types are less robust statistically.

Overall, although the three aerosol types yielded comparable results, differences remained in their specific RMSE, bias, and R^2 values. The MOD04-based type demonstrated the best performance across all three metrics, indicating higher accuracy, followed by Urban Clean, whereas the MOD09-based type exhibited the weakest performance across all indicators.

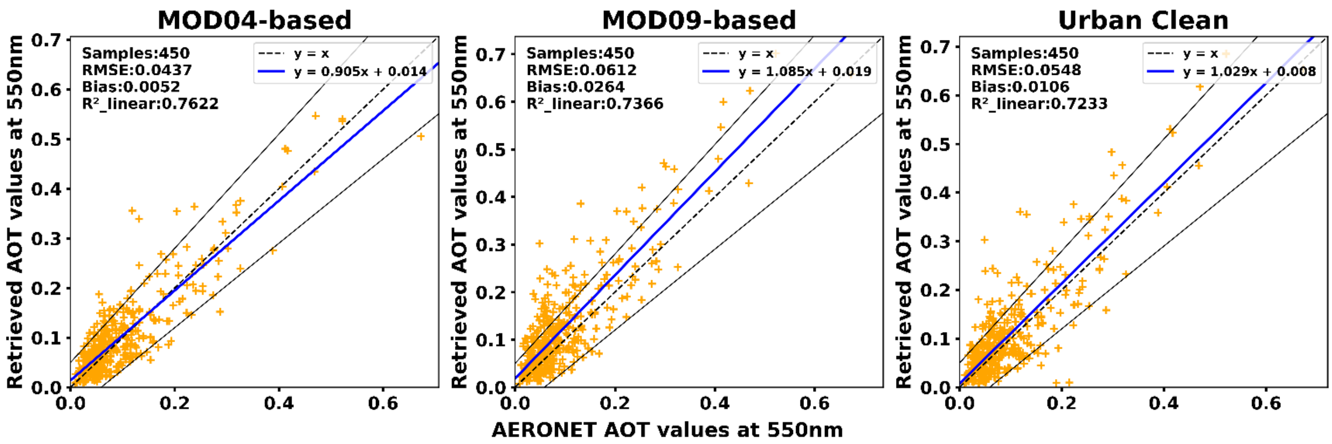

Figure 5: Dispersion plot of 550 nm aerosol optical thickness(specs=0.15×AOD550+0.05).

Table 4. Accuracy metrics for aerosol optical thickness.

	MOD04-based	MOD09-based	Urban Clean
RMSE	0.0437[0.0392, 0.0486]	0.0612 [0.0556, 0.0668]	0.0548 [0.0488, 0.0606]
R^2_AerT	0.7236 [0.6161, 0.8077]	0.4586 [0.2617, 0.6157]	0.5653 [0.3889, 0.6993]
Bias	0.0052 [0.0014, 0.0090]	0.0264 [0.0214, 0.0316]	0.0106 [0.0059, 0.0155]

Table 5. Statistical significance of differences in performance metrics among aerosol types (HOLM correction applied).

Comparison	Metric	Mean Diff	Holm-adjusted p	Significance
MOD04-based vs MOD09-based	Bias	−0.021232	0.00015	***
MOD04-based vs Urban Clean	Bias	−0.005385	0.00075	***
MOD09-based vs Urban Clean	Bias	0.015847	0.00010	***
MOD04-based vs MOD09-based	RMSE	-0.001839	0.00015	***
MOD04-based vs Urban Clean	RMSE	−0.001096	0.00010	***
MOD09-based vs Urban Clean	RMSE	0.000744	0.00030	***
MOD04-based vs MOD09-based	R2_AerT	0.257920	1.00000	ns
MOD04-based vs Urban Clean	R2_AerT	0.153634	1.00000	ns
MOD09-based vs Urban Clean	R2_AerT	−0.104286	0.94600	ns

Note: *** p < 0.001, ** p < 0.01, * p < 0.05, ns = not significant.

4.2 SR validation results

A total of 634 images were systematically analyzed to validate the SR accuracy. To maximize the utilization of all available pixels for validation, per-pixel cloud detection was performed on each image prior to accuracy assessment, and only cloud-free pixels were used for validation. Using predefined metric formulations, we calculated Accuracy-Precision-Uncertainty (APU) values by comparing the reflectance retrievals derived from the three dynamic aerosol types against the 6SV-simulated ground truth. For comparison, the same validation procedure was applied to the Landsat 8 LaSRC SR product to enable direct assessment of the algorithmic performance. To ensure a comprehensive evaluation, the results were presented across three analytical dimensions: overall, per band, and reflectance range assessments.

1)**Overall assessment**

The overall assessment was conducted by computing the total A, P, and U values of the four SR products. Table 6 presents the results. The total A, P, and U values for the four SR products are -0.0002975–0.0030145, 0.023184–0.026020, and 0.023366–0.26040, respectively.

Among these products, MOD04-based and Urban Clean exhibited a notably higher A value, indicating that the SR retrieved using these two dynamic aerosol types exhibited a higher systematic error, with a consistent offset across all observations. Regarding random error (P value) and overall accuracy (U value), the differences between the four SR products were minimal, indicating that their random errors and overall accuracies were comparable.

Using 95% confidence intervals, we formally assessed pairwise differences in A, P, and U across the four types. The confidence intervals for the between-type differences excluded zero, showing statistically significant disparities in all metrics. Despite exhibiting a certain degree of bias, The MOD04-based type had the lowest P (0.023184) and U (0.023366) values, indicating the most stable and least uncertain SR retrieval among the four products.

Table 6. Overall A, P, and U of four SR products.

	A (E-03)	P (E-02)	U (E-02)
MOD04-based	3.0145 [3.0111, 3.0178]	2.3184 [2.3181, 2.3186]	2.3366 [2.3310, 2.3418]
MOD09-based	0.7451 [0.7416, 0.7486]	2.4274 [2.4272, 2.4277]	2.4304 [2.4258, 2.4355]
Urban Clean	1.1465 [1.1431, 1.1500]	2.3870 [2.3872, 2.3877]	2.3911 [2.3857, 2.3963]
LaSRC	-0.2975 [-0.3013, -0.2937]	2.6020 [2.6017, 2.6022]	2.6040 [2.5966, 2.6112]

2)**Per-band assessment**

To visually assess the A, P, and U values of the SR across the seven bands for the four products, we computed the corresponding accuracy metrics (CI = 95%) and generated a heatmap (Fig. 6). The heatmap uses color intensity to intuitively display value magnitudes, with darker shades representing lower values and greater accuracy.

For A values, heatmap analysis indicated that MOD04-based, MOD09-based, Urban Clean, and LaSRC vary across different spectral bands. Specifically, MOD04-based had the smallest A values in the first and second bands, MOD09-based performed best in the third band, and LaSRC outperformed the others in the fourth to seventh bands. The A-value evaluation results were consistent with the overall assessment phase, indicating that MOD09-based and LaSRC demonstrated lower systematic errors compared to MOD04-based and Urban Clean. The P and U values follow a similar pattern, showing a decreasing trend with increasing wavelength. Specifically, the MOD04-based type demonstrated a higher accuracy in the visible bands (first to fourth bands), Urban Clean performed better in the NIR band (fifth band), whereas LaSRC exhibited superior performance in the SWIR bands (sixth and seventh bands).

In general, the per-band assessment provided a more detailed extension of the overall results. Notably, the four SR products exhibited substantial differences in systematic error (A value), with each product showing strengths in different spectral bands. In contrast, differences in random error (P value) and overall accuracy (U value) were relatively minor, indicating comparable retrieval performance among the products. MOD04-based showed the largest overall systematic error, with superior performance limited to the deep blue and blue bands. MOD09-based and Urban Clean exhibited similar accuracy across all metrics. LaSRC demonstrated the lowest A, P, and U values in the shortwave bands, suggesting a clear advantage in that spectral region.

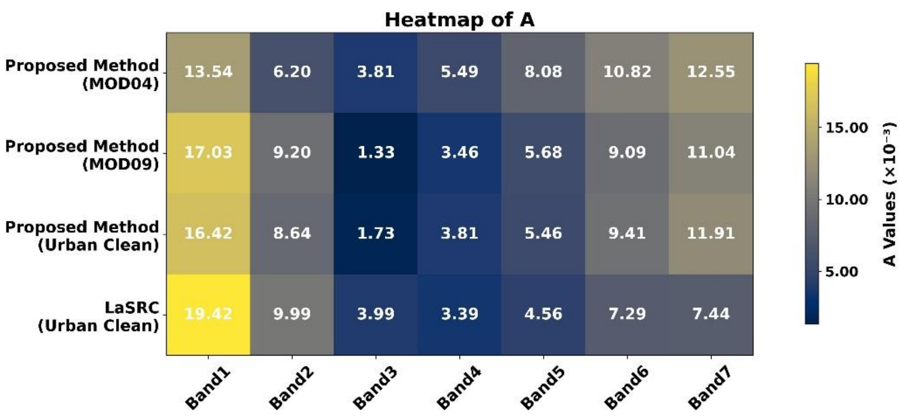

(a) A values of four SR products in single bands

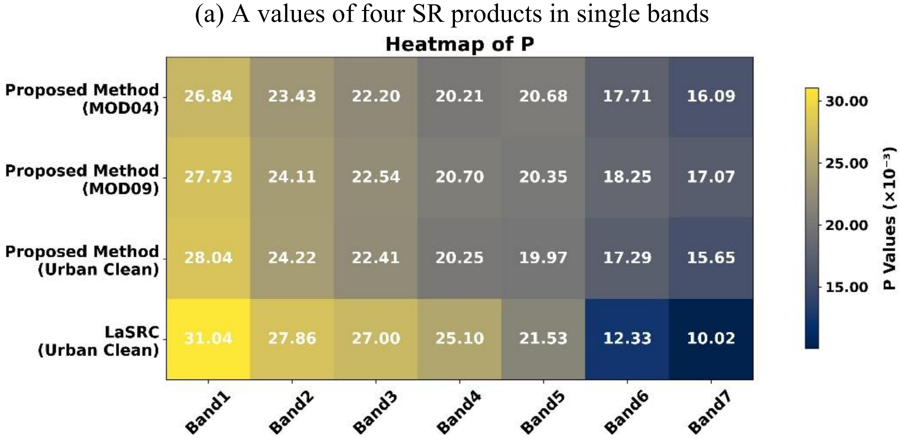

(b) P values of four SR products in single bands

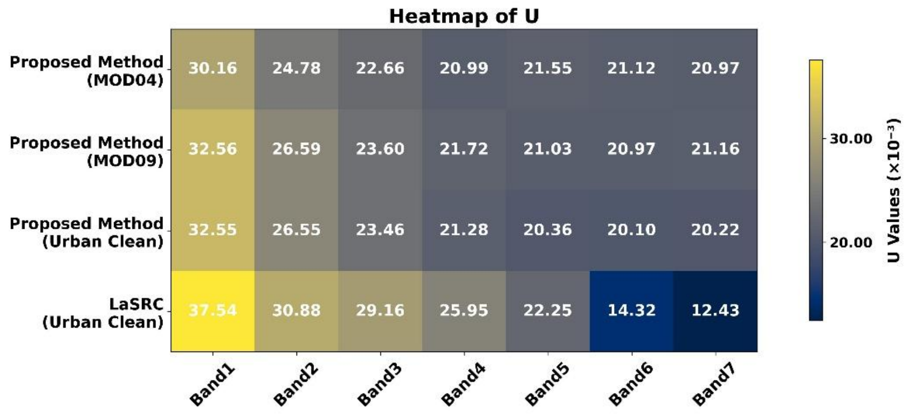

(c) U values of four SR products in single bands

Figure 6: Thermal map of the A, P, and U of four SR products in single bands.

3) **Reflectance-range assessment**

To further analyze the accuracy of SR, the 0–1 reflectance range was divided into 0.05 intervals, and accuracy metrics were computed for each interval to validate SR across the full range (CI = 95%). Fig. 7 illustrates the results: the x-axis represents SR values ranging from 0 to 1 with intervals of 0.2, the left y-axis denotes the number of pixels (with log-scale ticks at 10^4, 10^5, 10^6, 10^7, and 10^8), and the right y-axis presents accuracy metrics (A, P, and U). Gray bars denote pixel counts per interval, while red, green, and blue dashed lines represent A, P, and U, respectively. The purple dashed line represents the error line, defined as: $S\_line = 0.15 \times \rho + 0.015$.

As shown in Fig. 7, all products exhibited similar pixel distribution patterns. Most pixels were concentrated in the 0–0.3 reflectance range, especially in low-to-medium ranges across all bands. Therefore, subsequent analysis focused on this range to reflect the dominant pixel distribution and ensure robust SR performance evaluation.

In this section, we categorize the spectral bands based on the overall and per-band assessments. Using the accuracy validation metrics and error lines shown in Fig. 7, SR performance was analyzed for VIS (bands 1–4), NIR (band 5), and SWIR (bands 6 and 7).

VIS bands: Within the visible spectral bands, the A, P, and U values for all four products generally increased with SR, indicating amplified systematic errors, random errors, and total uncertainties at higher reflectance levels. However, performance variations among the products highlight common trends and distinct characteristics in SR retrieval.

The A values for most algorithms remained below the error thresholds across the 0–0.45 reflectance range, with relatively flat curves showing a peak interval near 0.25–0.30. During this phase, the deep blue and blue bands exhibit higher A values than the other visible bands. Beyond 0.45, A increased monotonically. LaSRC exhibited the most pronounced upward trend, consistently yielding higher A values than the other algorithms, indicating a greater systematic bias under high-reflectance conditions. MOD09-based and Urban Clean showed similar behavior, with deep blue/blue band A values largely below thresholds, whereas green/red bands displayed significant deviations above thresholds at reflectance >0.8 (except for the

MOD09-based in the red band). MOD04-based maintained stability up to 0.8 reflectance but showed a sharp A value spike near 0.85, surpassing MOD09-based and Urban Clean.

The P values in the VIS bands followed smooth trajectories with three distinct peaks. The first two peaks occurred at 0.15–0.20 and 0.25–0.30, predominantly in the deep blue and blue bands. MOD04-based type achieved lower and more stable P values in these ranges, whereas MOD09-based and Urban Clean type exhibited higher peaks, indicating weaker control over random errors. LaSRC exhibited the highest second peak in the deep blue bands, reflecting significant random errors. A third abrupt P-value increase emerges near 0.6 reflectance, with error magnitudes increasing with wavelength. MOD04-based displays minimal increments, exceeding thresholds only in the green/red bands, while MOD09-based and Urban Clean display comparably higher peaks across broader reflectance ranges. The P values of LaSRC persistently exceeded the thresholds above a reflectance of 0.5, indicating severe random errors. Notably, MOD04-based, MOD09-based, and Urban Clean surpassed the error thresholds in the high-reflectance range (>0.8).

Mirroring P value trends, U values peak at 0.15–0.20 reflectance in deep blue/blue bands for MOD04-based, MOD09-based, and Urban Clean, with LaSRC showing negligible peaks. The MOD04-based minimal peaks confirm the superior precision of the low-reflectance regimes. All the algorithms exhibited monotonically increasing U values with reflectance. MOD04-based excelled in the low-to-moderate range, whereas MOD09-based and Urban Clean stabilized at higher reflectance. LaSRC performed the worst above 0.8 reflectance, with markedly elevated U values.

Overall, in the VIS bands, the MOD04-based type achieved optimal A/P/U performance in the low-to-moderate reflectance range, whereas the MOD09-based type minimized errors at high reflectance. Urban Clean metrics closely aligned with MOD09-based metrics but were marginally higher. The LaSRC product demonstrated the largest errors across the VIS bands and did not exhibit any advantages in these spectral ranges.

NIR bands: In the NIR band, all four products exhibited an overall increasing trend in A, P, and U values with increasing SR.

The MOD04-based, MOD09-based, and Urban Clean-based A values exhibited peak values in the high SR range. MOD04-based peaks at reflectance values between 0.90 and 0.95, with A values in the other intervals remaining within the expected error limits. In comparison, both the MOD09-based and Urban Clean peaks were approximately 0.85–0.90 and maintained stable A values across ranges, indicating robust control of systematic errors in the NIR band. Meanwhile, the LaSRC exhibited a sharp increase above 0.75 reflectance, exceeding the expected error threshold.

Regarding to P values, MOD04-based, MOD09-based, and Urban Clean all showed a monotonically increasing trend, exceeding the expected error limits when the SR surpassed 0.80. The MOD04-based type, in particular, showed relatively higher P values in the high-reflectance ranges, suggesting significant random errors. MOD09-based performs similarly to Urban Clean, with a slight advantage over Urban Clean in some ranges (0.55–0.75). LaSRC exhibits distinct interval-based characteristics. The P values were lower than those of the other algorithms in the low-reflectance range (0.15–0.45), indicating relatively small random errors. However, the P values rise sharply beyond the 0.6–0.65, exceeding the error threshold, but then become the lowest in high-reflectance regions (above 0.85), where random errors are well controlled.

The U values of MOD04-based, MOD09-based, and Urban Clean followed a similar trend, displaying small peaks at medium (~0.60) and high (~0.90) reflectance levels, surpassing the expected error limits when the SR exceeded 0.85. This indicates that the overall error increased for these three methods in the medium-to high-reflectance range. In contrast, LaSRC demonstrated a distinct monotonic increase in U values, exceeding the expected error limits over a wide range (above 0.6) and considerably higher than those of the other three methods, revealing notable deficiencies in the control of both random and systematic errors.

Overall, the findings for the NIR bands were consistent with those for the VIS bands. The MOD04-based type demonstrated superior performance in low-to-medium reflectance regions with the lowest A, P, and U values. The MOD09-based type effectively controlled systematic and random errors in high-reflectance ranges, whereas Urban Clean achieved the lowest A, P, and U values at SR levels of approximately 0.5 and 0.8. LaSRC exhibited relatively low errors only within a certain low-reflectance range of the NIR bands.

SWIR bands: The A, P, and U values of the four products remained more stable in the SWIR bands than in the other bands. In general, the A, P, and U values exhibited a slow upward trend with SR while remaining within the expected error range. This indicates that the processing methods for the SWIR bands can effectively control the errors under different reflectance conditions, particularly in the high-reflectance range.

For the A values, the MOD04-based, MOD09-based, and Urban Clean types exhibited similar trends, with a distinct trough around an SR of 0.3, indicating smaller systematic errors in low-reflectance regions. In contrast, the A-value curve from LaSRC remained relatively flat, suggesting more stable systematic errors, particularly in the high-reflectance ranges. Specifically, in Band 6, the MOD04-based type demonstrated outstanding performance in the low-reflectance range, with smaller systematic errors, whereas in the mid-to-high reflectance range, the Urban Clean type consistently maintained low systematic errors. In Band 7, although MOD09-based showed some advantages in the extremely low reflectance range (<0.1) and MOD04-based performed well in the low-reflectance region (0.1 – 0.4), LaSRC exhibited a superior ability to control systematic errors over a broader range, particularly in high-reflectance ranges.

The P-value trends of MOD04-based, MOD09-based, and Urban Clean show notable similarity, with distinct peaks emerging in the 0.35–0.40 and 0.85–0.90 reflectance ranges. These peaks indicate increased random errors and reduced error control capabilities within these intervals. In contrast, LaSRC demonstrated more stable P-value curves with minimal random errors and the lowest data dispersion at low reflectance levels (<0.3).

The U-value curves exhibited morphological similarities to the P-value curves across all four products, demonstrating a gradual decline in overall accuracy as SR increased, accompanied by two minor peaks in the U-value curves. For Band 6, MOD04-based showed a relative advantage only within the 0–0.1 reflectance range, while Urban Clean achieved superior performance in moderate-to-high reflectance intervals (0.45–0.85), exhibiting the smallest random errors and higher overall accuracy. LaSRC excels in low-reflectance ranges (0.1 – 0.45) with minimal errors and the lowest data dispersion. For Band 7, LaSRC outperformed all other products across all SR ranges, particularly under high-SR conditions, where it achieved markedly better retrieval accuracy, demonstrating its strong performance in SWIR-band retrieval.

Overall, in SWIR Band 6, each product exhibits distinct advantages at specific reflectance intervals. MOD04-based and MOD09-based types performed well in the 0–0.1 and 0.85–1.0 ranges, while Urban Clean excelled in the mid-to-high reflectance region, exhibiting the lowest random errors. LaSRC stands out in the low-reflectance range, demonstrating a lower uncertainty. For Band 7, LaSRC consistently outperformed the other algorithms across all SR intervals at the 2.1 μm wavelength, exhibiting the lowest overall error.

The following conclusions were drawn from the aforementioned analysis of SR results across different aerosol types, spectral bands, and reflectance intervals: The MOD04-based type exhibited smaller errors and higher overall accuracy in the VNIR bands; MOD09-based demonstrated superior performance in the high-reflectance ranges of the first six spectral bands with minimized errors; LaSRC showed notable superiority in the SWIR bands, particularly in Band 7 (2.1 μm), where both random and systematic errors were markedly lower than the other three products; while the Urban Clean type achieved high accuracy only in medium-reflectance regions near 1.6 μm (Band 6) but underperformed in other scenarios.

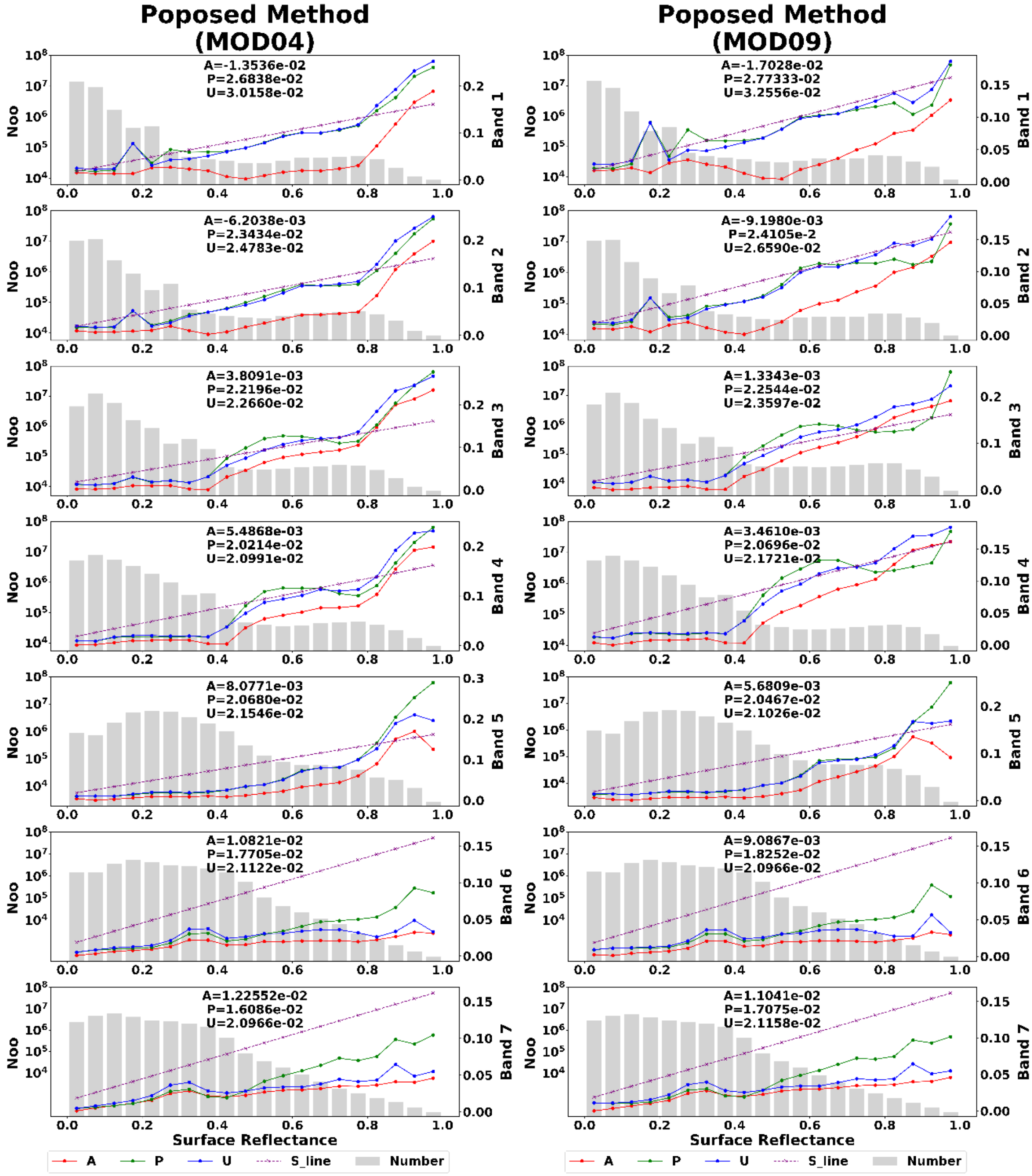
Poposed Method (MOD04)
Poposed Method (MOD09)
A=-1.3536e-02
P=2.6838e-02
U=3.0158e-02
A=-1.7028e-02
P=2.77333e-02
U=3.2556e-02
Band 1
A=-6.2038e-03
P=2.3434e-02
U=2.4783e-02
A=-9.1980e-03
P=2.4105e-2
U=2.6590e-02
Band 2
A=3.8091e-03
P=2.2196e-02
U=2.2660e-02
A=1.3343e-03
P=2.2544e-02
U=2.3597e-02
Band 3
A=5.4868e-03
P=2.0214e-02
U=2.0991e-02
A=3.4610e-03
P=2.0696e-02
U=2.1721e-02
Band 4
A=8.0771e-03
P=2.0680e-02
U=2.1546e-02
A=5.6809e-03
P=2.0467e-02
U=2.1026e-02
Band 5
A=1.0821e-02
P=1.7705e-02
U=2.1122e-02
A=9.0867e-03
P=1.8252e-02
U=2.0966e-02
Band 6
A=1.22552e-02
P=1.6086e-02
U=2.0966e-02
A=1.1041e-02
P=1.7075e-02
U=2.1158e-02
Band 7
Noo
Surface Reflectance
A
P
U
S_line
Number

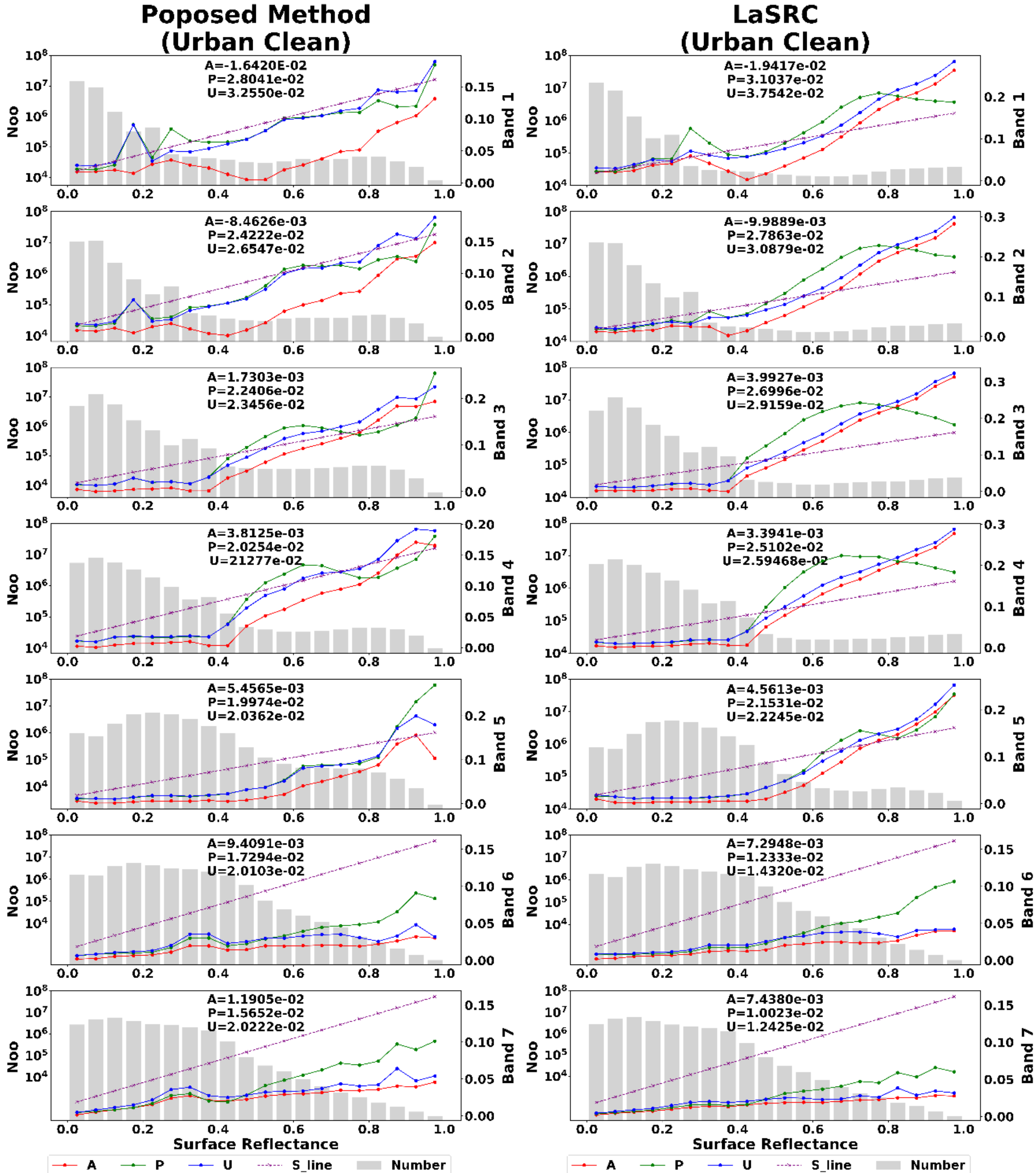

Figure 7: Number of pixels (left y-axis) and accuracy metrics (A, P, and U; right y-axis) of the four SR products across different SR intervals (0–1 with a step of 0.1).

4) **Landcover SR assessment**

To evaluate SR accuracy for different land surface types, land-cover samples were derived from a subset of Landsat 8 scenes randomly selected from the 634 scenes used for SR validation. Representative pixels for each surface type were extracted from these images using RSEIs, including NDBI, NDSI, NDVI, NDWI, and BSI, ensuring more than 5,000 sample points for each type. The performance of the four SR products was assessed using RMSE and bias across seven spectral bands, as shown in Fig. 8 (RMSE) and Fig. 9 (bias).

Overall, the SR retrieval performance exhibits distinct spectral behaviors across different surface types. Vegetation and water both show an overall decreasing RMSE trend from the short-wavelength bands to the longer-wavelength bands, with higher errors concentrated in the VIS bands and substantially reduced errors toward the SWIR region. The decrease is more continuous for water, while vegetation shows a relatively sharp reduction after the short-wavelength region and then remains at a low-error level. Snow presents the strongest spectral variability, with relatively high RMSE in the VIS bands, followed by a marked decrease toward the SWIR region. Soil shows a clear reduction in RMSE from the blue band to the VIS bands, after which the errors remain relatively low with slight spectral fluctuations. Building surfaces exhibit moderate spectral variability, with lower RMSE generally observed in the middle VIS bands and increased errors toward both the blue band and the longer-wavelength bands.

Bias analysis further reveals strong reflectance-dependent characteristics. High-reflectance surfaces, especially snow and building surfaces, tend to exhibit positive Bias values in longer wavelengths, indicating overestimation. Low-reflectance surfaces, including soil, vegetation, and water, are predominantly underestimated in the VIS bands, although the magnitude and sign of Bias vary across wavelengths and products. The detailed comparisons for each surface type are discussed below.

Building: Building surfaces show moderate retrieval errors across bands, with RMSE reaching minimum values around Bands 3–4 and increasing again toward longer wavelengths. Among the four products, MOD04-based generally show lower RMSE in the VIS bands, while the differences among products are relatively small around Bands 3–4. LaSRC exhibits the largest RMSE in Band 1 but becomes comparable to other products in longer wavelengths and shows relatively low RMSE in Band 7. MOD09-based and Urban Clean shows moderate RMSE in the VIS bands and remains comparable to the other products in the SWIR region.

Bias results indicate that all products exhibit wavelength-dependent transitions. Underestimation dominates in Bands 1–2, while overestimation becomes evident from Band 3 onward. MOD04-based retrievals present the lowest Bias magnitudes in the first two bands, while LaSRC shows lower Bias magnitudes in the remaining bands. In contrast, MOD09-based and Urban Clean retrievals generally exhibit Bias values comparable to those of MOD04-based throughout the spectrum.

Snow: Snow surfaces exhibit relatively large retrieval errors in the VNIR region compared with their performance at longer wavelengths. RMSE values peak around Bands 2–4 and decrease rapidly toward Bands 6–7. MOD04-based achieves the lowest RMSE across nearly all bands, indicating the most stable performance over snow surfaces. MOD09-based and Urban Clean show intermediate RMSE in the VNIR bands, whereas LaSRC exhibits larger RMSE in Bands 1–5. In Bands 6–7, the RMSE values of all products converge to relatively low levels.

Bias values for snow are predominantly positive across most bands, indicating systematic overestimation, except for slight negative or near-zero values in some longer wavelengths. The magnitude of Bias peaks in Bands 2–4 and decreases substantially toward longer wavelengths. MOD04-based generally exhibits the smallest Bias magnitude across most bands, while LaSRC show larger positive Bias in the VNIR region.

Soil: Soil surfaces demonstrate the most stable SR retrieval performance across spectral bands. RMSE values decrease rapidly from Band 1 to Band 3 and remain relatively low afterward. Among the four products, Urban Clean achieves low RMSE in the VIS bands, while LaSRC shows the lowest or near-lowest RMSE in several longer-wavelength bands. MOD09-based shows intermediate performance over soil surfaces. MOD04-based exhibits consistently higher RMSE than the other three products, indicating reduced stability over soil surfaces.

Bias results show that soil is generally underestimated in the VIS bands, with Bias gradually increasing toward zero or slight overestimation in longer wavelengths. Urban Clean and LaSRC maintain Bias values closer to zero across several middle and longer-wavelength bands, while MOD04-based exhibits stronger underestimation, especially in Bands 1–4.

Vegetation: Vegetation surfaces show high RMSE in Band 1, followed by a sharp decrease toward Band 3 and relatively stable performance thereafter. MOD04-based retrievals achieve the lowest RMSE in the first three bands and remain comparable to Urban Clean and LaSRC in the SWIR region. The other three products exhibit broadly similar RMSE patterns, with only slight band-dependent differences. Specifically, MOD09-based shows the lowest RMSE in the fifth band, Urban Clean performs better in the SWIR bands, and LaSRC is close to Urban Clean overall while achieving the lowest RMSE in the fourth band.

Bias results indicate strong underestimation in Bands 1–2 for all products. The Bias gradually approaches zero or slightly positive values in longer wavelengths. Urban Clean and MOD09-based maintain relatively small Bias magnitudes in several longer-wavelength bands, while MOD04-based shows slightly larger positive Bias in Bands 5–6.

Water: Water surfaces exhibit improved retrieval accuracy with increasing wavelength. RMSE values are lowest in Bands 6–7 for all products, while VIS bands show larger retrieval errors. MOD04-based achieves the lowest or near-lowest RMSE in Bands 1–4, indicating strong capability in VIS retrieval over water. Urban Clean achieves low RMSE in the longer wavelengths, particularly in the SWIR region, although differences among products become small in Bands 6–7. MOD09-based and LaSRC retrievals both exhibit significantly higher RMSE across the first five bands, whereas their RMSE values converge with those of the other products in the SWIR bands.

Bias analysis shows that most products exhibit underestimation in the VIS bands, especially in Bands 1–2. The Bias magnitude generally decreases toward longer wavelengths, approaching near-zero values in Bands 6–7. MOD04-based and LaSRC generally maintain smaller Bias magnitudes in several VIS bands, whereas Urban Clean show near-zero Bias in longer wavelengths.

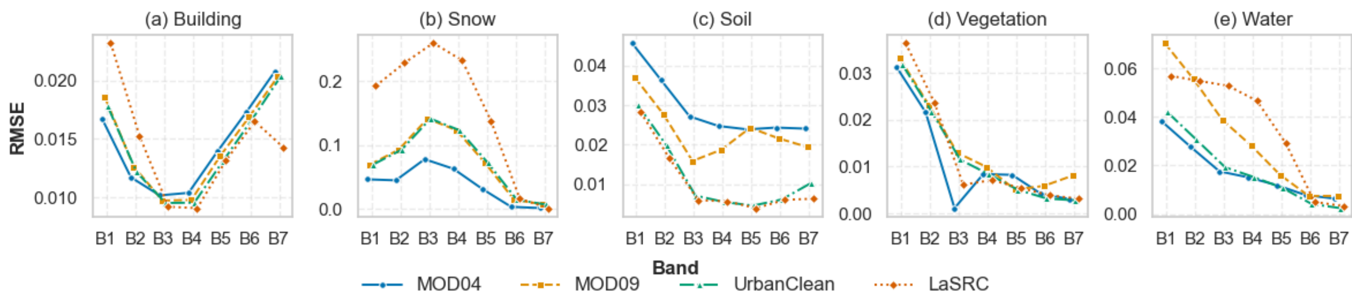

Figure 8: RMSE of the four SR products across seven spectral bands.

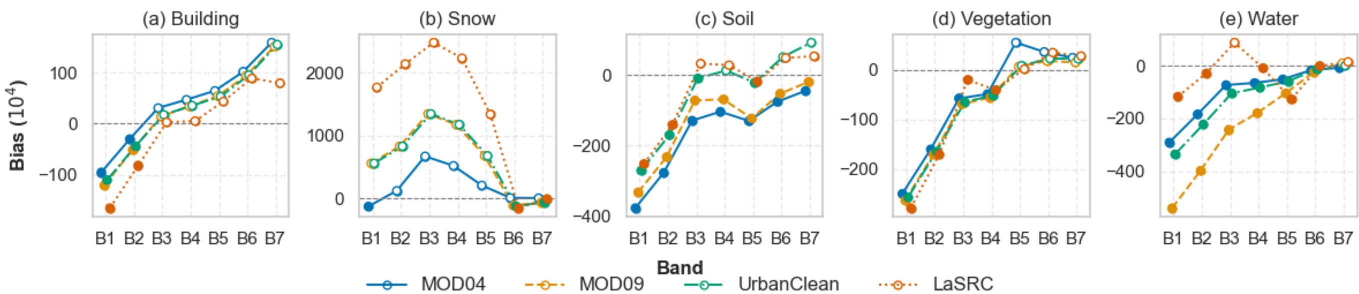

Figure 9: Bias of the four SR products across seven spectral bands.

5 Discussions

5.1 AOD retrievals

The scatter plots and regression analyses presented in Fig. 5 show clear differences in AOD retrieval performance among the three aerosol types. MOD04-based retrievals generally align more closely with AERONET observations, with a larger proportion of points falling within the empirical uncertainty range. Urban Clean performs moderately, while MOD09-based exhibits greater dispersion and systematic deviations. Statistical analyses of RMSE and Bias indicate that these differences are significant, confirming that MOD04-based retrievals outperform the other two types under the evaluated conditions.

The superior performance of MOD04-based type can be attributed to its dynamic aerosol subtype-selection mechanism, which incorporates seasonal and geographic information. For a fixed location and season, MOD04 typically selects the same aerosol type for the majority of images, with only a very small fraction of images near type boundaries exhibiting two aerosol types. As a result, the continuity of AOD retrieval is generally closer to actual atmospheric conditions. In contrast, MOD09-based subtype selection, which is based on the residual-minimization criterion, is more likely to result in images in which multiple aerosol types are present. Examination of the AOD subtype results indicates that fine-scale, pixel-level mixtures of multiple aerosol types do not occur within individual images, while the presence of two aerosol types across the image is relatively common, with each subtype distributed over multiple contiguous pixels, forming extended continuous regions. To mitigate this, an overall smoothing process was applied to the AOD results, which may have contributed to the larger errors observed for the MOD09 type.

Urban Clean employs a single aerosol classification, limiting its adaptability under variable atmospheric conditions. While its retrievals are generally more consistent than MOD09-based ones in some cases, they are less accurate than MOD04-based when actual aerosol properties diverge from the assumed type. These patterns suggest that physically informed aerosol subtype selection, with spatial and temporal variability, is crucial for achieving accurate AOD retrieval.

Several limitations of the current study should be acknowledged. First, the analysis is based on a single year and 465 AOD data points from AERONET, covering diverse climate types globally, limits both the spatial coverage of sites and the overall dataset size. In results, the robustness of AOD retrieval has not been assessed across a wider range of locations or with larger datasets, potentially restricting the generalizability of the findings. In addition, most AERONET observations correspond to AOD values below 0.2, indicating higher aerosol loading or partially cloud-obscured conditions less frequently recorded. Consequently, the performance of AOD retrieval under elevated aerosol loading, as well as under extreme surface conditions such as snow, ice, or heterogeneous urban areas, remains largely untested due to the limited representation of these scenarios in the current dataset.

Future research should extend these evaluations to multi-year datasets to better assess seasonal and interannual variations in AOD retrieval performance, and incorporating additional high-quality AOD datasets beyond AERONET could provide broader coverage of atmospheric conditions and improve the generalizability of findings.

5.2 SR retrievals

Based on the validation results and preliminary conclusions across the four SR products under different spectral bands and full-range reflectance intervals, we conducted an in-depth investigation of the underlying causes of performance disparities during SR inversion. Leveraging the validation data from Fig. 7, the analysis primarily investigated performance discrepancies among the products, focusing on variations across spectral bands and reflectance intervals, while also assessing their similarities.

1) **Similar trends**

The vertical analysis in Fig. 7 reveals consistent trends in the accuracy metrics (A, P, and U) across all four products. With increasing wavelength from the VIS to SWIR bands, all three metrics generally decreased, indicating an overall improvement in SR retrieval accuracy. In the VNIR bands, especially in the deep-blue and blue bands, the A, P, and U values were relatively large, and some high-reflectance intervals exceeded the expected error limits, indicating stronger retrieval uncertainties at shorter wavelengths. By contrast, the SWIR bands showed more stable performance, with all APU values remaining within the expected error limits. These trends can be attributed mainly to wavelength-dependent aerosol effects. Shorter wavelengths are more sensitive to aerosol scattering and AOD uncertainty, so residual errors in aerosol estimation can be amplified in the deep-blue and blue bands. Conversely, weaker aerosol scattering and reduced sensitivity to AOD uncertainty in the SWIR bands lead to more stable SR retrieval and lower uncertainty.

Horizontal analysis showed a systematic increase in A, P, and U with increasing SR across all products (Fig. 7), indicating reduced retrieval accuracy under high-reflectance conditions. This behavior may be related to the characteristics of bright and heterogeneous surfaces, such as snow, bright bare soil, urban surfaces, and mixed pixels. These surfaces are more likely to exhibit strong subpixel heterogeneity and anisotropic reflectance behavior, which can enhance bidirectional reflectance distribution function (BRDF) and adjacency effects and increase the influence of shadows and mixed pixels. These effects can influence the estimation of path radiance and atmospheric transmittance, thereby increasing the discrepancy between retrieved and reference SR.

2) **Different performance**

The validation results revealed distinct performance variations among the four SR products.

MOD04-based: The MOD04-based type demonstrated superior retrieval accuracy in the VNIR bands across moderate-to-low reflectance ranges, outperforming the other products. This advantage is likely due to the incorporation of region- and season-specific aerosol parameters, which enhance aerosol subtype selection and optimize AOD retrieval. Because aerosol scattering effects are stronger at shorter wavelengths, inaccuracies in aerosol characterization can propagate more directly into SR retrievals in the VNIR region. This effect is particularly evident over moderate-to-low reflectance surfaces, where even small AOD retrieval errors may produce amplified SR deviations. Consequently, the MOD04-based SR product achieves higher accuracy in these bands and reflectance ranges, reflecting its ability to better represent spatiotemporal aerosol variability and reduce systematic biases under complex atmospheric conditions.

In summary, the MOD04-based type demonstrated exceptional inversion accuracy and generalizability in the VNIR bands under moderate-to-low reflectance scenarios, which can be attributed to its comprehensive consideration of the geographic and seasonal aerosol dynamics, making it a reliable reference for SR retrieval with broad potential for global-scale AC applications in the future.

MOD09-based: The validation results indicated that the SR product corresponding to the MOD09-based aerosol type performed exceptionally well in a relatively narrow high-reflectance range (>0.8). Across the first six bands examined in this study, although the errors for all four products exceeded the acceptable range in this interval, the MOD09-based type effectively controlled these errors and demonstrated a superior retrieval accuracy. This advantage can be attributed to the application of residual constraints during AOD retrieval, which enables effective error regulation, thereby improving the SR retrieval accuracy in high-reflectance ranges, particularly in remote sensing imagery of large-scale high-reflectance surfaces (e.g., snow). However, this residual-minimization strategy also carries certain risks. The introduction of residual constraints may cause abrupt changes in the subtypes of adjacent pixels, which may not reflect the reality for the spatial continuity of aerosol distributions. To mitigate the uncertainty resulting from these abrupt transitions, an overall smoothing process was applied to the AOD results. However, this approach has inherent limitations and may introduce additional small errors, which together contribute to the relatively moderate SR performance of the MOD09-based product outside the high-reflectance range. Consequently, future research should aim to enhance the spatial continuity of aerosol retrieval by investigating more appropriate smoothing strategies or alternative adjustment methods to minimize the potential adverse effects of these abrupt transitions on AOD and SR retrieval accuracies.

In conclusion, despite the exceptional performance of the MOD09-based aerosol type in high-reflectance ranges, making it a valuable tool for processing remote sensing images with extreme SR conditions, its subtype selection method under residual constraints is associated with certain risks.

Urban Clean: Among the four SR products, the one using the Urban Clean aerosol type, a subtype of the MOD09-based aerosol type integrated into the LaSRC algorithm, exhibited the weakest overall performance. It demonstrates limited advantages only at specific intervals, such as the moderate reflectance ranges in band 6, with generally inferior inversion accuracy compared with other products. Its error patterns partially align with the MOD09-based aerosol type but remain systematically less robust. This underperformance likely stems from the specialized design as a subtype of the MOD09-based design, which is optimized for urban areas with low air quality and stringent application constraints. Consequently, their narrow applicability limits their global utility, particularly in heterogeneous environments.

In summary, although Urban Clean shows localized efficacy, its restricted operational scope and demanding implementation criteria render it non-competitive with other types of global SR inversion tasks.

LaSRC product: The LaSRC product demonstrated marked superiority in the SWIR bands, especially in Band 7 (2.1 μm), where its SR estimates exhibited enhanced precision and reliability. This advantage is amplified with increasing reflectance levels, which is likely attributable to the refined handling of water vapor and other absorptive gases that critically influence the SWIR bands. The LaSRC algorithm effectively mitigates atmospheric interference, enabling high-fidelity retrieval in these spectral ranges. Notably, its performance surpassed that of the other products in high-reflectance SWIR scenarios.

However, LaSRC exhibits elevated error levels in the VNIR bands. The A-value (systematic bias) consistently exceeded that of the other products, suggesting pronounced deviations. This discrepancy may originate from two aspects: 1. the residual quality control method used in LaSRC, which flags pixels failing band 4/5/7 spectral tests as water bodies, potentially propagating AOD retrieval errors into VNIR reflectance estimates, and 2. the atmospheric parameters in the LaSRC method interpolated using AOD via cubic spline functions, which may introduce errors.

In conclusion, although the excellent performance of LaSRC in the SWIR band highlights its potential for high-precision reflectance retrieval, its systematic VNIR errors require further investigation to guide the refinement of algorithms.

These comparisons revealed the underlying factors contributing to the differences in product performance, such as the adaptability of MOD04-based aerosol parameterization. These insights offer practical guidance for optimizing the selection of dynamic aerosol types based on scene characteristics and highlight the potential advantage of the LaSRC algorithm in improving reflectance accuracy through a more effective correction of absorptive gas effects.

Several limitations of the current study should be acknowledged. The analysis is based on a relatively limited dataset of 634 Landsat 8 scenes, and the AERONET stations used for validation are generally located in open areas to ensure reliable measurements. As a result, the spatial distribution of validation sites is constrained, providing representativeness primarily at the level of climate zones but not capturing all land-cover types. Although some urban sites are included, complex surfaces such as dense forests, snow/ice-covered areas, and heterogeneous urban regions remain underrepresented. Expanding the dataset in future work could improve the generalizability of SR validation across a wider range of surface types.

3) **SR retrievals with different landcover**

Fig. 8–9 indicate that SR retrieval accuracy exhibits clear spectral dependence that varies with surface type. For soil, vegetation, and water, retrieval errors generally decrease toward longer wavelengths despite slight spectral fluctuations, indicating improved SR retrieval accuracy from the blue/VIS bands to the NIR and SWIR regions. In contrast, building and snow exhibit non-monotonic spectral behavior, with building errors lower in the middle VIS bands and snow errors increasing within the VIS region before decreasing toward longer wavelengths. These variations reflect the combined effects of aerosol scattering, surface spectral characteristics, BRDF effects, subpixel heterogeneity, and the signal strength of different land-cover types.

For soil surfaces, SR retrievals show relatively stable spectral behavior. Soil spectra typically vary smoothly with wavelength and often exhibit comparatively homogeneous spatial distributions. Although soil reflectance is influenced by mineral composition, organic matter, and moisture content, these factors usually introduce gradual spectral variations, which favor stable AC performance. Among the four products, Urban Clean and LaSRC generally demonstrate stable behavior over soil surfaces, with Urban Clean showing low RMSE in the VIS bands and LaSRC showing strong performance in several longer-wavelength bands. In contrast, the MOD04-based and MOD09-based types, both of which involve dynamic aerosol subtype selection, do not show consistent advantages over soil surfaces. This may be because, for surfaces with smooth spectral signatures and relatively stable reflectance behavior, additional aerosol subtype selection may introduce variability in aerosol optical properties without providing clear compensating benefits. Such variability can perturb path-radiance and atmospheric-transmittance correction, especially in the short visible bands, leading to larger RMSE or stronger Bias compared with the more stable Urban Clean and LaSRC products. Therefore, the weaker performance of MOD04-based and the limited advantage of MOD09-based over soil suggest that the benefit of dynamic aerosol subtype selection is surface- and wavelength-dependent.

For vegetation and building surfaces, retrieval performance is strongly influenced by surface complexity. Vegetation canopies consist of multilayer structures with strong anisotropic reflectance, while urban areas contain diverse materials and complex geometric configurations. These characteristics increase spatial heterogeneity and anisotropic reflectance behavior, which can amplify BRDF effects, adjacency effects, shadow-related uncertainties, and mixed-pixel contamination, thereby increasing AC uncertainty. MOD04-based shows advantages in the deep-blue and blue bands for these complex surfaces, especially for vegetation and building pixels in the short-wavelength region. This may be related to its aerosol subtype selection scheme that incorporates seasonal and geographic variability, which can better represent aerosol optical properties under conditions where short-wavelength SR retrieval is highly sensitive to aerosol scattering. In contrast, MOD09-based uses an error-minimization-based subtype selection strategy. Although this strategy can be effective in some retrieval conditions, it may not always provide additional advantages over spectrally complex surfaces because the selected aerosol subtype may be optimized for retrieval residuals rather than for land-cover-specific SR behavior. Urban Clean and LaSRC show relatively stable performance in the NIR and SWIR regions for several land-cover types. As aerosol scattering effects weaken with increasing wavelength, AC becomes less sensitive to aerosol-type selection, and stable aerosol assumptions can provide consistent retrieval behavior. This may explain why Urban Clean performs well in the NIR and SWIR regions for vegetation and water surfaces, and why LaSRC remains competitive in longer wavelengths. In contrast, multi-subtype selection strategies used in MOD04-based and MOD09-based may introduce additional variability when the sensitivity of SR retrieval to aerosol-type differences is reduced.

For water and snow surfaces, SR retrieval is strongly affected by their extreme reflectance characteristics. Water surfaces are characterized by very low reflectance, weak surface signals, and additional variability caused by surface roughness, adjacency effects, and specular reflection, all of which can increase retrieval uncertainty, especially in the VIS bands. Snow surfaces, on the other hand, exhibit extremely high reflectance in the VIS region and strong directional reflectance effects, which may increase retrieval sensitivity and introduce systematic biases. Among the four products, MOD04-based demonstrates stable performance over snow surfaces and in the VIS bands for water pixels, likely benefiting from its geographically and seasonally constrained aerosol parameterization in short-wavelength regions. Urban Clean shows advantages over water surfaces in longer wavelengths, reflecting its stability in spectral regions less sensitive to aerosol scattering. MOD09-based generally exhibits larger retrieval variability over snow and water surfaces, suggesting that its subtype selection based on retrieval-error minimization may be less stable under extreme reflectance conditions. LaSRC maintains competitive accuracy in longer wavelengths, but shows relatively larger deviations over high-reflectance snow surfaces and low-reflectance water surfaces in the VIS region.

Overall, the analysis indicates that aerosol treatment strategies play a critical role in determining SR retrieval performance across different surface types. Physically constrained and seasonally/geographically adaptive aerosol schemes, such as MOD04-based types, demonstrate improved robustness in short-wavelength bands and under temporally varying conditions, while stable single-type assumptions provide more consistent performance over smoother surfaces or in spectral regions with reduced aerosol sensitivity. The performance of each aerosol type is not uniform across land-cover types, but depends on the combined effects of wavelength, SR magnitude, surface structural complexity, and aerosol sensitivity.

However, the current SR analysis over different landcover still has several inherent limitations. Both the 30-meter spatial resolution of Landsat 8 and the inherent uncertainties associated with extracting land-cover types using empirically derived RSEIs limit the accuracy of SR validation across different surface types. Although approximately 5,000 pixels were used in the analysis, this sample size remains insufficient to fully represent all land-cover types. Additionally, vegetation and snow surfaces exhibit pronounced seasonal and interannual variability, which was not explicitly stratified in the current study and may influence aerosol-type performance. The current results provide preliminary evidence of these effects, as MOD04-based aerosol types consistently achieve lower RMSE and Bias over snow surfaces and demonstrate advantages over vegetation in several short-wavelength bands. These patterns likely reflect the MOD04-based aerosol subtype selection scheme, which incorporates geographical and seasonal information, enabling better adaptation to temporally varying surface–atmosphere conditions. A more comprehensive assessment would require finer land-cover classification, explicit temporal stratification, and an expanded dataset. Future work could therefore involve validation using more refined land-cover products and larger pixel samples to further evaluate SR performance across surface types with pronounced temporal variability.

5.3 Recommendations for Aerosol-Type Selection

Based on the validation results for AOD and SR, the following operational guidelines were proposed for selecting the dynamic aerosol types (MOD04-based, MOD09-based, and Urban Clean):

a) MOD04-based aerosol type is recommended for AOD retrieval across extensive and topographically complex regions. Its adaptive parameterization scheme, which incorporates seasonal- and geographical-dependent aerosol properties, ensures better alignment with surface typologies, thereby delivering higher retrieval accuracy. However, the MOD04-based type may systematically overestimate AOD in scenes with high AOD levels. To mitigate this bias, global linear correction should be implemented for such datasets to enhance the reliability of the results.

b) When retrieving SR data from commonly used VNIR four-band remote sensing imagery such as China's Gaofen-1 (Lu et al., 2015) and Gaofen-2 (Huang et al., 2018), we recommend using the MOD04-based dynamic aerosol type. This type exhibited higher retrieval accuracy for medium- to low-reflectance pixels in the VNIR bands. Given the predominance of such pixels in remote-sensing imagery, the MOD04-based type offers notable advantages for surface-reflectance retrieval in VNIR applications.

c) When retrieving SR data from remote sensing imagery containing extensive high-reflectance terrain features, we recommend using the MOD09-based dynamic aerosol type. This approach employs the residual minimization principle to constrain errors, and demonstrates superior performance in the inversion of high-reflectance surfaces. In particular, for extensive high-reflectance features such as snow-covered areas and urban structures, the MOD09-based type effectively enhances the inversion accuracy and provides more reliable SR estimates.

The following recommendations were proposed for LaSRC products: In remote sensing applications that rely on SWIR bands, such as snow/ice detection and land-cover change monitoring, the LaSRC product should be prioritized as the data source. Its higher accuracy in the SWIR-band SR estimation provides more reliable spectral information, thereby enhancing the scientific validity and operational reliability of related applications.

It is worth noting that, while our recommendations are derived under relatively homogeneous atmospheric conditions, the complex variability of real-world environments means they should only serve as one criterion for aerosol type selection. In practical applications, users should combine multiple indicators and data-driven considerations to make final choices.

Table 7. Performance summary of four processing strategies for AOD and SR retrieval.

	MOD04-based	MOD09-based	Urban Clean	LaSRC
AOD retrieval	Best	Lower	Moderate	-
SR retrieval	Best in VNIR	Best in high-reflectance	Similar to MOD09-based, slightly worse	Best in SWIR
SR by land cover type	Water, snow	normal	Vegetation, building	Vegetation, building

6 Conclusions

This study derived AOD and SR data from Landsat 8 imagery across 100 global sites for the year 2022 through AC using three dynamic aerosol types (MOD04-based, MOD09-based, and Urban Clean).

The results were validated against ground truth measurements. For AOD evaluation, a comparative analysis of three aerosol treatment strategies was conducted using linear regression analysis and accuracy metrics, demonstrating the strong performance of the MOD04-based type. In the comparative analysis of SR products, the official Landsat 8 LaSRC product was included, and the accuracy of four SR products was evaluated across the full reflectance range using three performance metrics (A, P, and U). The validation results indicate that the MOD04-based type achieved high retrieval accuracy in the VNIR spectral bands. The MOD09-based type demonstrated relatively strong performance in high-reflectance conditions. The Urban Clean type yielded performance comparable to MOD09-based in certain reflectance ranges but showed limited advantages overall. The LaSRC product exhibited clear strengths in the SWIR region, particularly around 2.1 μm, while maintaining competitive performance in other bands.

The land cover–based analysis reveals that SR retrieval performance varies with surface spectral characteristics and structural complexity. For soil surfaces, LaSRC demonstrates strong performance across spectral bands. For vegetation and building surfaces, Urban Clean shows stable behavior in the middle bands, while MOD04-based provides improved performance in the deep-blue and blue bands. For water and snow surfaces, MOD04-based demonstrates stable performance in the VIS bands, whereas Urban Clean shows advantages in longer wavelengths. MOD09-based generally exhibits larger retrieval variability across surface conditions.

The analyses from the perspectives of performance metrics and land cover types exhibit both consistency and complementarity. Both approaches reveal similar spectral performance patterns, such as the strong VIS-band performance of MOD04-based and the SWIR advantages of LaSRC. Meanwhile, the land cover–based evaluation highlights the influence of surface characteristics on retrieval behavior. For example, Urban Clean shows relatively stable performance in the NIR region for vegetation and building surfaces. In contrast, MOD09-based demonstrates greater variability across reflectance conditions, and its advantages in high-reflectance conditions are not consistently observed across different surface environments. These results suggest that SR retrieval performance is influenced by the combined effects of spectral characteristics, reflectance magnitude, and surface structure. The agreement and divergence between the two evaluation perspectives provide a more comprehensive understanding of retrieval performance.

Notably, the current conclusions were derived from existing sites and datasets. In practical applications, a more in-depth analysis and specific processing strategies are required, considering diverse scenarios and image characteristics. In addition, the present study utilized only one year of remote sensing data, which provides valuable insights but may limit the generalizability of the conclusions. Therefore, subsequent studies should expand the validation not only to additional geographical regions and land cover types but also to multi-year datasets, thereby capturing seasonal and interannual variations. Further spatially explicit analyses of aerosol subtype occurrence and its impacts on AOD and SR retrievals would also be valuable for better understanding the mechanisms underlying the performance differences among dynamic aerosol types. By increasing the sample size and data diversity, we would help assess aerosol-type performance across various environmental conditions thereby enhancing its global applicability and reliability.

Furthermore, the observed superiority of the LaSRC algorithm in the SWIR bands, particularly near 2.1 μm, warrants mechanistic investigation. Future studies should focus on elucidating the physical and algorithmic foundations of these advantages. Through targeted optimization of LaSRC SWIR-band reflectance retrieval workflows, we sought to advance the accuracy of large-scale surface monitoring and explore its broader application potential in multi-sensor remote sensing.

Code and data availability

The code used in this study is not publicly available due to commercial considerations. The datasets used in this work are publicly available remote sensing and ground-based observation products. Satellite data were obtained from the Landsat 8 mission provided by the United States Geological Survey (USGS) Earth Resources Observation and Science (EROS) Center. Aerosol optical depth data were obtained from the Aerosol Robotic Network (AERONET) database. These datasets can be accessed through the official USGS and AERONET websites. Further information about the datasets used in this study can be provided by the authors upon reasonable request.

Author contributions

Shuning Zhang conducted the experiments and wrote the manuscript. Hao Zhang designed the study and provided supervision. Bing Zhang contributed to the scientific guidance of the study. Zhenzhen Cui performed the data preprocessing. All authors reviewed and approved the final manuscript.

Competing interests

The authors declare that they have no conflict of interest.

Acknowledgements

The authors acknowledge the U.S. Geological Survey (USGS) for providing the Landsat 8 SR data and the NASA Goddard Space Flight Center and the contributing principal investigators for the AERONET data used in this study. The authors would also like to express their sincere gratitude to the anonymous reviewers for their constructive comments and suggestions, which greatly helped improve the quality and clarity of this manuscript.

Financial support

This work was supported by the Deep Earth Probe and Mineral Resources Exploration - National Science and Technology Major Project of China(2024ZD1002100) and the National Natural Science Foundation of China (41771397).

References

Ångström, A.: The parameters of atmospheric turbidity, Tellus, 16, 64–75, https://doi.org/10.1111/j.2153-3490.1964.tb00144.x, 1964.

Anderson, G. P., Pukall, B., Allred, C. L., Jeong, L. S., Hoke, L. M., Chetwynd, J. H., Adler-Golden, S. M., Berk, A., Bernstein, L. S., Bernstein, S. C., Acharya, P. K., and Matthew, W. M.: FLAASH and MODTRAN4: state-of-the-art atmospheric correction for hyperspectral data, 1999 IEEE Aerosp. Conf. Proc., 4, 177–181, https://doi.org/10.1109/AERO.1999.792088, 1999.

Berk, A., Bosch, J., Hawes, F., Perkins, T., Conforti, P. F., Anderson, G. P., Kennett, R. G., and Acharya, P. K.: MODTRAN® 6.0 User's Manual, Air Force Res. Lab., 2018.

Brazile, J., Richter, R., Schläpfer, D., Schaepman, M. E., and Itten, K. I.: Cluster versus grid for operational MODTRAN-based look-up table generation of ATCOR tables, Parallel Comput., 34, 32–46, https://doi.org/10.1016/j.parco.2007.11.002, 2008.

Chen, L., Wang, R., Fei, Y., Fang, P., Zha, Y., and Chen, H.: Multi-angle aerosol optical depth retrieval method based on improved surface reflectance, Atmos. Meas. Tech., 17, 4411–4430, https://doi.org/10.5194/amt-17-4411-2024, 2024.

Lu, C., and Bai, Z.: Characteristics and typical applications of GF-1 satellite, 2015 IEEE Int. Geosci. Remote Sens. Symp. (IGARSS), 1246–1249, https://doi.org/10.1109/IGARSS.2015.7325999, 2015.

Doxani, G., Vermote, E. F., Roger, G. C., Skakun, S., Gascon, F., Collison, A., Keukelaere, L. D., Desjardins, C., Frantz, D., Hagolle, O., Kim, M., Louis, J., Pacifici, F., Pflug, B., Poilvé, H., Ramon, D., Richter, R., and Yin, F.: Atmospheric correction inter-comparison exercise (ACIX-II Land): An assessment of atmospheric correction processors for Landsat-8 and Sentinel-2 over land, Remote Sens. Environ., 285, 113412, https://doi.org/10.1016/j.rse.2022.113412, 2023.

Dubovik, O., Smirnov, A., Holben, B. N., King, M. D., Kaufman, Y. J., Eck, T. F., and Slutsker, I.: Accuracy assessments of aerosol optical properties retrieved from Aerosol Robotic Network (AERONET) Sun and sky radiance measurements, J. Geophys. Res. Atmos., 105, 9791–9806, https://doi.org/10.1029/2000JD900040, 2000.

Dubovik, O., Holben, B. N., Eck, T. F., Smirnov, A., Kaufman, Y. J., King, M. D., Tanré, D., and Slutsker, I.: Variability of absorption and optical properties of key aerosol types observed in worldwide locations, J. Atmos. Sci., 59, 590–608, 2002.

Dwyer, J. L., Roy, D. P., Sauer, B., Jenkerson, C. B., Zhang, H. K., and Lymburner, L.: Analysis ready data: enabling analysis of the Landsat archive, Remote Sens., 10, 1363, https://doi.org/10.1175/1520-0469(2002)059<0590:VOAAOP>2.0.CO;2, 2018.

Eck, T. F., Holben, B. N., Reid, J. S., O'Neill, N. T., Schafer, J. S., Dubovik, O., Smirnov, A., Yamasoe, M. A., and Artaxo, P.: High aerosol optical depth biomass burning events: a comparison of optical properties for different source regions, Geophys. Res. Lett., 30, https://doi.org/10.1029/2003GL017861, 2003.

Foga, S., Scaramuzza, P. L., Guo, S., Zhu, Z., Dilley, R. D., Beckmann, T., Schmidt, G. L., Dwyer, J. L., Hughes, M. J., and Laue, B.: Cloud detection algorithm comparison and validation for operational Landsat data products, Remote Sens. Environ., 194, 379–390, https://doi.org/10.1016/j.rse.2017.03.026, 2017.

Friedl, M. A., McIver, D. K., Hodges, J. C. F., Zhang, X. Y., Muchoney, D., Strahler, A. H., Woodcock, C. E., Gopal, S., Schneider, A., Cooper, A., Baccini, A., Gao, F., and Schaaf, C.: Global land cover mapping from MODIS: algorithms and early results, Remote Sens. Environ., 83, 287–302, https://doi.org/10.1016/S0034-4257(02)00078-0, 2002.

Gao, B. C., Heidebrecht, K. B., and Goetz, A. F. H.: Atmospheric removal program (ATREM) user's guide, Center Study Earth Space, Univ. Colorado, Boulder, 1992.

Gathman, S. G.: Optical properties of the marine aerosol as predicted by a BASIC version of the Navy Aerosol Model, Naval Res. Lab. Rep., 1983.

Giles, D. M., Sinyuk, A., Sorokin, M. S., Schafer, J. S., Smirnov, A., Slutsker, I., Eck, T. F., Holben, B. N., Lewis, J., Campbell, J., Welton, E. J., Korkin, S., and Lyapustin, A.: Advancements in the Aerosol Robotic Network (AERONET) Version 3 database, Atmos. Meas. Tech., 12, 169–209, https://doi.org/10.5194/amt-12-169-2019, 2019.

Grey, W. M. F., North, P. R. J., Los, S. O., and Mitchell, R. M.: Aerosol optical depth and land surface reflectance from multi-angle AATSR measurements, IEEE Trans. Geosci. Remote Sens., 44, 2184–2197, https://doi.org/10.1109/TGRS.2006.872079, 2006.

Guanter, L., Richter, R., and Kaufmann, H.: On the application of the MODTRAN4 atmospheric radiative transfer code to optical remote sensing, Int. J. Remote Sens., 30, 1407–1424, https://doi.org/10.1080/01431160802438555, 2009.

Holben, B. N., Eck, T. F., Slutsker, I., Tanré, D., Buis, J. P., Setzer, A., Vermote, E. F., Reagan, J. A., Kaufman, Y. J., Nakajima, T., Lavenu, F., Jankowiak, I., and Smirnov, A.: AERONET – a federated instrument network and data archive for aerosol characterization, Remote Sens. Environ., 66, 1–16, https://doi.org/10.1016/S0034-4257(98)00031-5, 1998.

Hall, D. K. and Riggs, G. A.: Normalized-difference snow index (NDSI), in: Encyclopedia of Snow, Ice and Glaciers, edited by: Singh, V. P., Singh, P., and Haritashya, U. K., Springer Netherlands, Dordrecht, 779–780, https://doi.org/10.1007/978-90-481-2642-2_376, 2011.

Hsu, N. C., Jeong, M. J., Bettenhausen, C., Sayer, A. M., Hansell, M., Seftor, C. S., Huang, J., and Tsay, S. C.: Enhanced Deep Blue aerosol retrieval algorithm: the second generation, J. Geophys. Res. Atmos., 118, 9296–9315, https://doi.org/10.1002/jgrd.50712, 2013.

Huang, W., Sun, S., Jiang, H., Gao, C., and Zong, X.: GF-2 satellite 1 m/4 m camera design and in-orbit commissioning, Chin. J. Electron., 27, 1316–1321, https://doi.org/10.1049/cje.2018.09.018, 2018.

Ichoku, C., Remer, L. A., Kaufman, Y. J., Levy, R., Chu, D. A., Tanré, D., and Holben, B. N.: MODIS observation of aerosols and estimation of aerosol radiative forcing over southern Africa during SAFARI 2000, J. Geophys. Res. Atmos., 108, https://doi.org/10.1029/2002JD002366, 2003.

Kaufman, Y. J., Tanré, D., Remer, L. A., Vermote, E. F., Chu, A., and Holben, B. N.: Operational remote sensing of tropospheric aerosol over land from EOS moderate resolution imaging spectroradiometer, J. Geophys. Res. Atmos., 102, 17051–17067, https://doi.org/10.1029/96JD03988, 1997.

Levy, R. C., Remer, L. A., and Dubovik, O.: Global aerosol optical properties and application to Moderate Resolution Imaging Spectroradiometer aerosol retrieval over land, J. Geophys. Res. Atmos., 112, https://doi.org/10.1029/2006JD007815, 2007a.

Levy, R. C., Remer, L. A., Mattoo, S., Vermote, E. F., and Kaufman, Y. J.: Second-generation operational algorithm: Retrieval of aerosol properties over land from inversion of Moderate Resolution Imaging Spectroradiometer spectral reflectance, J. Geophys. Res. Atmos., 112, https://doi.org/10.1029/2006JD007811, 2007b.

Levy, R. C., Remer, L. A., Tanré, D., Kaufman, Y. J., Ichoku, C., Holben, B. N., Livingston, J. M., Russell, P. B., and Maring, H.: Evaluation of the Moderate Resolution Imaging Spectroradiometer (MODIS) retrievals of dust aerosol over the ocean during PRIDE, J. Geophys. Res. Atmos., 108, https://doi.org/10.1029/2002JD002460, 2003.

Li, Z., Xu, H., Li, K. T., Li, D. H., Xie, Y. S., Li, L., Zhang, Y., Gu, X. F., Zhao, W., Tian, Q. J., Deng, R. R., Su, X. L., Huang, B., Qiao, Y. L., Cui, W. Y., Hu, Y., Gong, C. L., Wang, Y. Q., Wang, X. F., Wang, J. P., Du, W. B., Pan, Z. Q., Li, Z. Z., and Bu, D.: Comprehensive study of optical, physical, chemical, and radiative properties of total columnar atmospheric aerosols over China: An overview of Sun–Sky Radiometer Observation Network (SONET) measurements, Bull. Am. Meteorol. Soc., 99, 739–755, https://doi.org/10.1175/BAMS-D-17-0133.1, 2018.

Longtin, D. R., Shettle, E. P., Hummel, J. R., and Pryce, J. D.: A wind-dependent desert aerosol model: radiative properties, Air Force Geophys. Lab., 1988.

Lyapustin, A., Wang, Y., Korkin, S., and Huang, D.: MODIS collection 6 MAIAC algorithm, Atmos. Meas. Tech., 11, 5741–5765, https://doi.org/10.5194/amt-11-5741-2018, 2018.

Lyapustin, A., Zhao, F., and Wang, Y.: A comparison of multi-angle implementation of atmospheric correction and MOD09 daily surface reflectance products from MODIS, Front. Remote Sens., 2, 712093, https://doi.org/10.3389/frsen.2021.712093, 2021.

Maciel, D. A., Pahlevan, N., Barbosa, C. C. F., Novo, E. M. L. M., Paulino, R. S., Martins, V. S., Vermote, E. F., and Crawford, C. J.: Validity of the Landsat surface reflectance archive for aquatic science: Implications for cloud‐based analysis, Limnol. Oceanogr. Lett., 8, 850–858, https://doi.org/10.1002/lol2.10344, 2023.

Mann, J., Maddox, E., Shrestha, M., Irwin, J., Czapla-Myers, J., Gerace, A., Rehman, E., Raqueno, N., Coburn, C., Byrne, G., Broomhall, M., and Walsh, A.: Landsat-8 and 9 underfly international surface reflectance validation collaboration, Remote Sens., 16, 1492, https://doi.org/10.3390/rs16091492, 2024.

Masek, J. G., Vermote, E. F., Saleous, N. E., Wolfe, R., Hall, F. G., Huemmrich, K. F., Gao, F., Kutler, J., and Lim, T. K.: A Landsat surface reflectance dataset for North America 1990–2000, IEEE Geosci. Remote Sens. Lett., 3, 68–72, https://doi.org/10.1109/LGRS.2005.857030, 2006.

McFeeters, S. K.: The use of the normalized difference water index (NDWI) in the delineation of open water features, Int. J. Remote Sens., 17, 1425–1432, https://doi.org/10.1080/01431169608948714, 1996.

Meghraj, K. C., Leigh, L., Pinto, C. T., and Kaewmanee, M.: Method of validating satellite surface reflectance product using empirical line method, Remote Sens., 15, 2240, https://doi.org/10.3390/rs15092240, 2023.

Miller, C. J.: Performance assessment of ACORN atmospheric correction algorithm, Proc. SPIE, 4725, 438–449, https://doi.org/10.1117/12.478777, 2002.

Mueller-Wilm, U., Devignot, O., and Pessiot, L.: Sen2Cor configuration and user manual, ESA, 2017.

Pashayi, M., Satari, M., and Shahraki, M. M.: Multi-layer retrieval of aerosol optical depth in the troposphere using SEVIRI data, Atmos. Meas. Tech., 18, 1415–1439, https://doi.org/10.5194/amt-18-1415-2025, 2025.

Perkins, T., Adler-Golden, S., Cappelaere, P., and Mandl, D.: High-speed atmospheric correction for spectral image processing, Proc. SPIE, 8390, 246–252, https://doi.org/10.1117/12.918908, 2012a.

Perkins, T., Adler-Golden, S., Matthew, M. W., Berk, A., Bernstein, L. S., Lee, J., and Fox, M.: Speed and accuracy improvements in FLAASH atmospheric correction of hyperspectral imagery, Opt. Eng., 51, 111707, https://doi.org/10.1117/1.OE.51.11.111707, 2012b.

Radosavljevic, V., Vucetic, S., and Obradovic, Z.: Aerosol optical depth retrieval by neural networks ensemble with adaptive cost function, Proc. 10th Int. Conf. Eng. Appl. Neural Netw., 266–275, 2007.

Remer, L. A., and Kaufman, Y. J.: Dynamic aerosol model: urban/industrial aerosol, J. Geophys. Res. Atmos., 103, 13859–13871, https://doi.org/10.1029/98JD00994, 1998.

Remer, L. A., Kaufman, Y. J., Tanré, D., Mattoo, S., Chu, D. A., Martins, J. V., Li, R. R., Ichoku, C., Levy, R. C., Kleidman, R. G., Eck, T. F., Vermote, E. F., and Holben, B. N.: The MODIS aerosol algorithm, products, and validation, J. Atmos. Sci., 62, 947–973, https://doi.org/10.1175/JAS3385.1, 2005.

Richter, R., Louis, J., Muller-Wilm, U., Laroque, C., and Dingeldey, C.: Sentinel-2 MSI Level 2A Products Algorithm Theoretical Basis Document Issue: 2.0, ESA, 2012.

Richter, R., and Schläpfer, D.: Atmospheric and topographic correction (ATCOR theoretical background document), DLR IB, 1, 0564–03, 2019.

Rikimaru, A., Roy, P. S., and Miyatake, S.: Tropical forest cover density mapping, Trop. Ecol., 43, 39–47, 2002.

Rouse, J. W., Haas, R. H., Schell, J. A., and Deering, D. W.: Monitoring vegetation systems in the Great Plains with ERTS, in: Third Earth Resources Technology Satellite-1 Symposium, NASA SP-351, Vol. 1, 309–317, 1974.

Roy, D. P., Ju, J., Kline, K., Scaramuzza, P. L., Kovalskyy, V., Hansen, M., Loveland, T., Vermote, E. F., and Zhang, C.: Web-enabled Landsat Data (WELD): Landsat ETM+ composited mosaics of the conterminous United States, Remote Sens. Environ., 114, 35–49, https://doi.org/10.1016/j.rse.2009.08.011, 2010.

Roy, D. P., Wulder, M. A., Loveland, T. R., Woodcock, C. E., Allen, R. G., Anderson, M. C., Helder, D., Irons, J. R., Johnson, D. M., Kennedy, R., Scambos, T. A., Schaaf, C. B., Schott, J. R., Sheng, Y., Vermote, E. F., Belward, A. S., Bindschadler, R., Cohen, W. B., Gao, F., Hipple, J. D., Hostert, P., Huntington, J., Justice, C. O., Kilic, A., Kovalskyy, V., Lee, Z. P., Lymburner, L., Masek, J. G., McCorkel, J., Shuai, Y., Trezza, R., Vogelmann, J., Wynne, R. H., and Zhu, Z.: Landsat-8: science and product vision for terrestrial global change research, Remote Sens. Environ., 145, 154–172, https://doi.org/10.1016/j.rse.2014.02.001, 2014.

Satheesh, S. K., and Moorthy, K. K.: Radiative effects of natural aerosols: a review, Atmos. Environ., 39, 2089–2110, 2005.

Schläpfer, D., and Richter, R.: Geo-atmospheric processing of airborne imaging spectrometry data. Part 1: parametric orthorectification, Int. J. Remote Sens., 23, 2609–2630, https://doi.org/10.1080/01431160110115825, 2002.

She, L., Li, Z., Leeuw, G., Wang, W., Wang, Y., Yang, L., Feng, Z., Yang, C., and Shi, Y.: Time series retrieval of multi-wavelength aerosol optical depth by adapting Transformer (TMAT) using Himawari-8 AHI data, Remote Sens. Environ., 305, 114115, https://doi.org/10.1016/j.rse.2024.114115, https://doi.org/10.1016/j.rse.2024.114115, 2024.

She, L., Zhang, H. K., Bu, Z., Shi, Y., Yang, L., and Zhao, J.: A Deep-Neural-Network-Based Aerosol Optical Depth (AOD) Retrieval from Landsat-8 Top of Atmosphere Data, Remote Sens., 14, 1411, https://doi.org/10.3390/rs14061411, 2022.

Shettle, E. P., and Fenn, R. W.: Models for the Aerosols of the Lower Atmosphere and the Effects of Humidity Variations on Their Optical Properties, Air Force Geophys. Lab., 1979.

Staenz, K., and Williams, D.: Retrieval of surface reflectance from hyperspectral data using a look-up table approach, Can. J. Remote Sens., 23, 354–368, https://doi.org/10.1080/07038992.1997.10855221, 1997.

Staenz, K., Szeredi, T., and Schwarz, J.: ISDAS – a system for processing and analyzing hyperspectral data, Can. J. Remote Sens., 24, 99–113, https://doi.org/10.1080/07038992.1998.10855230, 1998.

Superczynski, S. D., Kondragunta, S., and Lyapustin, A. I.: Evaluation of the multi‐angle implementation of atmospheric correction (MAIAC) aerosol algorithm through intercomparison with VIIRS aerosol products and AERONET, J. Geophys. Res. Atmos., 122, 3005‐3022, https://doi.org/10.1002/2016JD025720, 2017.

Takamura, T., Nakajima, T., and SKYNET Community Group: Overview of SKYNET and its activities, Opt. Pura Apl., 37, 3303–3308, 2004.

Toller, G., Isaacman, A., Kuyper, J., and Toller, G.: MODIS Level 1B Product User's Guide for Level 1B Version 6.1.0 (Terra) and Version 6.1.1 (Aqua), NASA MCST, 2009.

Vermote, E. F., Tanré, D., Deuze, J. L., Herman, M., and Morcrette, J. J.: Second Simulation of a Satellite Signal in the Solar Spectrum – Vector (6SV), Remote Sens. Environ., 58, 101–111, 1997.

Vermote, E. F., Tanré, D., Deuzé, J. L., Herman, M., Morcrette, J. J., and Kotchenova, S. Y.: Second simulation of a satellite signal in the solar spectrum – vector (6SV) user guide, version 3, Air Force Res. Lab., Hanscom AFB, MA, USA, 2006a.

Vermote, E. F., and Kotchenova, S.: Atmospheric correction for the monitoring of land surfaces, J. Geophys. Res. Atmos., 113, https://doi.org/10.1029/2007JD009662, 2008.

Vermote, E. F., and Saleous, N.: LEDAPS surface reflectance product description, Univ. Maryland, 1–21 pp., 2007.

Vermote, E. F., and Saleous, N.: Operational atmospheric correction of MODIS visible to middle infrared land surface data in the case of an infinite Lambertian target, Earth Sci. Satell. Remote Sens., 1, 123–153, https://doi.org/10.1007/978-3-540-37293-6_8, 2006b.

Vermote, E. F., Justice, C., Claverie, M., and Franch, B.: Preliminary analysis of the performance of the Landsat-8/OLI land surface reflectance product, Remote Sens. Environ., 185, 46–56, https://doi.org/10.1016/j.rse.2016.04.008, 2016.

World Meteorological Organization: Report of the expert meeting on aerosols and their climatic effects, WCP-55, Geneva, Switzerland, 1983.

World Meteorological Organization: A preliminary cloudless standard atmosphere for radiation computations, WCP-112, Geneva, Switzerland, 1986.

Zha, Y., Gao, J., and Ni, S.: Use of normalized difference built-up index in automatically mapping urban areas from TM imagery, Int. J. Remote Sens., 24, 583–594, https://doi.org/10.1080/01431160304987, 2003.

Zhang, B., Chen, Z., Peng, D., Benediktsson, J. A., Liu, B., Zou, L., Li, J., and Plaza, A.: Remotely sensed big data: evolution in model development for information extraction, Proc. IEEE, 107, 2294–2301, https://doi.org/10.1109/JPROC.2019.2948454, 2019.

Zhang, H., Yan, D., Zhang, B., Fu, Z., Li, B., and Zhang, S.: An operational atmospheric correction framework for multi-source medium-high-resolution remote sensing data of China, Remote Sens., 14, 5590, https://doi.org/10.3390/rs14215590, 2022.